INVESTIGATION OF A THREE-DIMENSIONAL DESIGN PROCEDURE FOR AXIAL FLOW PUMP IMPELLERS

Thesis by

Ray D. Bowerman

In Partial Fulfillment of the Requirements

for the Degree of

Mechanical Engineer

California Institute of Technology

Pasadena, California

1955

ACKNOWLEDGEMENTS

The writer would like to express his deepest appreciation to Dr. D. A. Morelli who initiated and guided this work.

The writer is also indebted to Dr. A. J. Acosta and to Professor A. Hollander for their interest and advice.

Acknowledgement is also made to the staff of the Hydrodynamics Laboratory of the California Institute ot Technology for assistance in the experimental work.

ABSTRACT

A design procedure for axial flow pump impellers is presented that accounts for induced interference effects in the prediction of performance. Induced interference velocities at an impeller blade have been calculated using a three-dimensional model that includes the effects of the other blades and of the total downstream vorticity along the centerline of the pump.

The design method considers improvement of cavitation conditions by specifying the radial variation of the design parameters such that the pressure distribuions on all radial sections are similar.

Experimental work on a two-bladed impeller has yielded results that give good support to all aspects of the design procedure.

TABLE OF CONTENTS

I. INTRODUCTION

In recent years, axial flow pump impellers have been designed by applying the data of two-dimensional isolated airfoil theory to each cylindrical section of a blade. In general the results have been good. However, there has been some disagreement and doubt as to the corrections that should be applied to the two-dimensional airfoil shapes when they are subjected to the influence of the cylindrical boundaries of the pump hub and pump case, and when there are mutual interference effects between the blades themselves. Previous attempts to account for interference have been based on calculations of simple cascades of airfoils in two dimensions. The present work involves a correction procedure which is based on a three-dimensional model.

A. Results Indicated by Existing Methods for Designing Pump Impellers

In the design procedure outlined by O'Brien and Folsom,[3]* airfoil data is employed in computing the characteristics of the pump wherein no allowance is made for mutual interference of the blades - - low solidity offered as justification. The pump tested had good performance and reasonably supported the method of design. However, cascade theories show that corrections to the isolated airfoil performance were in order. Spannhake[4] suggests use of the aerodynamic coefficients with cor-

* Numbers refer to references at the end of the text.

rections for mutual interference but suggests that better theories giving mutual interference coefficients should be developed.

Improved cascade results have been developed quite recently because of the interest in axial flow compressors. However, use of these modern theories for pump design is not immediately possible because the parameters involved have not been investigated either theoretically or experimentally for the values commonly found in the geometry of a pump impeller. Preliminary attempts to use cascade formulas for pumps have shown that difficulties arise in the extension of the cascade parameters, and generally the results given by cascade methods are not substantiated by existing pump design knowledge. The fact that cascade theories are quite useful in compressor design indicates that the differences in the geometries of pump impellers and compressor rotor rows are significant even though there is no direct indication from cascade theory that the differences are of importance. An analysis of these differences and of all theories is undertaken in the last section of the text.

In order to produce a theory that will give proper corrections for designing pump impellers, Spannhake[4] suggests that a three-dimensional model (i.e., blades treated as spokes of a wheel) be used as a basis of calculation wherein the blades are replaced by bound vortices which continue down the hub, and beyond the case.

B. Preliminaries to the Present Investigation

Following the general suggestions of Spannhake,[4] some theoretical and experimental work with three-dimensional considerations has been completed. In an experimental study of a single blade calculated with its downstream hub vorticity taken into account, it was established that the hub vorticity considered as a growth of circulation through the blade region and continuing downstream with constant value, properly predicts the attitude of the blade.[1] In fact, if half of the tangential velocity that must exist far downstream is considered to have occured at the blade region and if it is constant through the extent of the blade region, then the attitude of the blade is exactly as it would be in a cascade model where the vector mean of the upstream and downstream velocity vectors is taken as the blade attitude. However, in the work of Reference 1, the tangential velocity was not taken constant, but grew through the blade region with an average of one half the value downstream (it is assumed that the tangential velocity upstream is zero). For this case, the blade attitude remains the same as before but a correction to the camber must be made because the resultant streamline is curved. The streamline curvature was found to be a function of the blade axial extent divided by the radial position of the blade section considered. In the case of the one bladed impeller, the correction was quite small.

In the case of two or more blades, the mutual interference of the blades must also be considered. For this purpose, a three-dimensional solution for the flow field of a radial vortex element in an annular region has been presented by H. Tyson, Jr.[2].* It was expected that this solution could be used to represent a blade permitting calculation of the effects induced at various regions in the flow field. Unfortunately the series solution of this problem had slow convergence (diverged in the neighborhood of the vortex element) and calculation of the velocity values required considerable time. Consequently calculations were made for only a few geometric positions. Also this difficulty in calculation rendered the solution quite useless for further mathematical summation (as with a Green's function) for distributed vorticity representing a blade. Therefore the present interference calculation made use of a graphical summation of the velocities given by Tyson.

As the present interference calculation depends heavily on the work of Tyson, the essentials of that solution and resulting data and curves have been reproduced in Appendix II A.

C. Experimental Program

The evaluation of past theories has been handicapped by the lack of systematical experimental work on pump impellers. Tests on complete pumps do not reveal

* The solution was obtained by Professor W. D. Rannie.

which of the several factors determining performance are most important.

It would be advantageous to study the variations of the physical parameters and the real fluid effects separately. This is not possible; however, more complete knowledge of pump operation can be obtained by studying the components of the pump separately and by supplementing performance tests with internal flow measurements.

Such studies have been made on a two-vaned impeller designed by the present three-dimensional method. Although the design parameters were chosen in a somewhat arbitrary manner, the geometric quantities and resultant performance are reasonably representative of commercial practice. Experiments performed on the impeller determined the complete performance characteristics and yielded information including blade static head distributions and the effect of the real fluid.

The experimental work has been useful in giving insight into other aspects of impeller design that are not revealed directly in the theory. The problem of how successive cylindrical sections of an impeller blade should be related (i.e., the correct variation of design parameters with radius) has been partially clarified. Furthermore, knowledge of some of the factors affecting cavitation has been revealed.

II. THE INTERFERENCE CALCULATION

A. Summary of Design Procedure

The method of designing the impeller blades uses isolated airfoil theory (for which abundant theoretical and experimental information exists) with corrections resulting from three-dimensional calculations for the interference effects. Specifically, a camber line is fitted to a curving streamline in the annular blade region in the same manner that a camber line is placed on a straight streamline for an isolated airfoil in an infinite field of uniform flow. The performance of the designated camber line is then considered to be the same in both cases. The effect of thickness has been neglected. The main consideration then is to determine the streamline in the annular region of the impeller.

B. Factors Determining the Streamline

The streamline is determined by considering the through-flow velocity, the tangential velocity of the impeller, and the induced interference velocities. The through-flow velocity and the impeller velocity are constant and proportional to radius respectively. The interference velocities are dependent upon several factors: the hub ratio, the ratio of the blade axial extent to the tip radius, the blade angle, the circulation value, and the number of blades. Also, the interference velocities are

a function of the radius. The determination of the streamline primarily requires the summing of the induced interference velocities. Approximate methods only are possible.

C. Method of Summation - - Approximations

The procedure for finding the induced interference velocities acting upon a blade is to first consider the blade to be "removed". Then, the interference velocities induced in this region by the other blades making up the impeller and by the total downstream vorticity on the centerline of the pump are summed. This, in a sense, is equivalent to a two-dimensional lattice calculation for interference in which one blade of the infinite row is removed and the velocity field there due to the remainder of the blades is determined.

The total interference effect in a blade region is the sum of the interference from (1) the other blades directly, (2) the centerline downstream vorticity due to the other blades, (3) the centerline downstream vorticity of the "removed" blade, and (4) the cyclic effect of the "removed" blade upon itself. Items one and two above are obtained from Tyson's work (Appendix II) as an inseparable quantity that includes the effects of the boundaries. A correction of $\Gamma/2$ (per blade) has been added to achieve conditions of zero prewhirl and Γ total circulation downstream because Tyson considered symmetrical splitting of the radial vortex element, half upstream and half downstream.

Items three and four above cannot be handled easily as there is no exact way to separate the radial vortex element from the hub and case effects. There is doubt whether item four even exists as stated. In any event item four is small compared to items one, two, and three and has been omitted. Item three is approximated by the centerline vortex solution employed in Reference 1 and reviewed in Appendix II B. It is admitted that the contribution of the "removed" blade has been approximated.

In determining the interference velocities due to the other blades, only the tangential component was retained. The radial velocity component is quite small and tends to cancel in the vortex summations as it carries opposite sign either side of a singularity. Similarly the induced axial velocity component tends to cancel, even though it has magnitude equal to the tangential component. Where the solidity is small, the axial component is small compared to the total tangential component and so may be neglected without serious error. When the solidity becomes large and small blade angles are used, then neglecting the axial velocity may not be permissible.

D. Methods for Representing Blades

When the solidity of an impeller is quite small (few blades of short axial extent at a small blade angle), then, for calculation in the region of a "removed" blade, the other blades may be approximated by single vortices.

However, as the axial extent of the blades is increased (blade angle remaining the same) the solidity becomes larger and eventually some allowance must be made for the distribution of the bound vorticity. Ideally the vorticity is smeared out over the blade centerline with strength varying in accordance with the blade loading. A simpler representation is to disperse a few vortex elements with varying strength along the blade centerline. Where the calculating region is far away from the blade, the simpler blade representation introduces negligible error. The same average induced velocity is achieved even though the blade distribution is approximate.

As a limited amount of data was presented in Reference 2, only a poor approximation to the blade vorticity distribution was possible. The singularities could be set only at certain intervals along a single helical surface (corresponding to a blade angle of 32.4° at the hub and 20.9° at the case). Besides single vortex representation two other cases were summed: three dispersed vortices, and five dispersed vortices. Typical blade representations are shown in Figure 1 with the calculating regions indicated. These approximations are apparently satisfactory for the usual geometries of pump impellers. The calculating region is reasonably removed if only a few blades (up to six) of not excessive solidity are involved. Blade angles can be varied a little from the helical representation without serious changes in induced

velocities.

Small errors in the induced interference velocities resulting from the approximations in the calculating procedure are not serious. As the correction to the camber line due to the interference is about ten to twenty percent, then an error of as much as ten percent in the induced velocities is an error of only one to two percent in the final camber. Many other factors can give errors of this magnitude. The attitude of the blade is of importance as well as the amount of camber. The attitude is automatically taken care of in the present method and experiment shows that the result is good.

E. Interference Calculation Results

In Figure 1 examples of the blade representations are shown. Summations were made at the hub, mid-radius, and case corresponding to the radius ratios, $\eta = r/r_2$ of 0.6, 0.8, and 1.0. For calculating the total interference resulting from the number of blades on an impeller, the procedure is as follows: For a two bladed impeller, the calculating region is considered 180° from the other blade. For a three bladed pump the calculating region is 120° from two other blades either side of the "removed" blade. Therefore the velocity values at 120° either side of a blade representation, added together, give the desired total. Similar additions are made for greater numbers of blades. The final total interference is the sum of the

effects of the other blades and the downstream vorticity of the "removed" blade. The induced velocity contribution from the downstream vorticity is shown in Figure 2 for typical cases.

In Figure 3 values of the total tangential interference velocity are plotted against the axial blade extent ($\xi = z/r_t$) for the case of a two-vaned impeller with $\xi_t = 0.72$ and for a four-vaned impeller with $\xi_t = 0.4$ where ξ_t is the total axial extent of the blade.* The shape of these curves is typical of all cases summed. As the curves deviate only slightly from straight lines, each curve for the dimensionless induced tangential velocity (C_θ) was approximated by a line with the equation

$$C_\theta = K_o + K_1 \left(z/z_t \right) \qquad (1)$$

where K_o is the interference velocity value at the "removed" blade leading edge and K_1 is the difference in values between the trailing edge and leading edge. The value of z/z_t varies from 0 to 1 from the leading edge to trailing edge. In this manner, all of the cases have been reported by presenting values of the constants K_o and K_1. In Figure 4a the values of K_o and K_1 are tabulated, and in Figure 4b K_o and K_1 are plotted as functions of the radius ratio. The constants are given for various numbers of blades and for ratios of the axial extent to the case radius of $\xi_t = 0.2$, 0.4, 0.6, and 0.72. It should be

* A complete listing of the notation is found in Appendix I.

noted that C_θ is the dimensionless total interference velocity equal to $V_\theta r_2/\Gamma_b$ where V_θ is the total interference velocity and Γ_b is the value of circulation of a single blade. Γ_b is used because the number of blades is taken into account in the summation and so included in the values of K_0 and K_1.

F. Discussion of the Interference Calculation Results

It is of interest to note that the present interference calculation supports certain known limits concerning fluid flows. A check on cascade theory is the comparison of the case of infinite spacing to chord ratio with the isolated airfoil. In the three-dimensional calculation there cannot be a limit that corresponds to the isolated airfoil; however, the case of zero blades has a similar significance. In Figure 4c a plot of the K_0 and K_1 values are shown as functions of the number of blades on an impeller. It can be seen that K_0 and K_1 approach zero for zero blades corresponding to no interference effects.

The limit as the number of blades is increased is the Euler result for an infinite number of blades. This limit requires exact guidance of the flow, so the total circulation must be achieved at the impeller exit. In other words, the "interference" is the total effect of the impeller. Therefore K_0 must become zero and K_1 become equal to the total circulation velocity. It can

be seen (Figure 4c) that the K_o curves do seem to reach a maximum and begin to approach zero as the number of blades is increased. Similarly K_i appears to approach the total tangential circulation velocity. Figure 4c also shows that neither isolated airfoil data alone nor Euler theory can give correct results for designing pump impellers.

The effect of the axial extent of the blades is demonstrated in Figures 4b and 4c. If the axial extent is small, K_o is near to half the total circulation far downstream. K_o becomes smaller as the axial extent increases. On the other hand, as the axial extent gets small then K_i approaches zero and for large axial extent K_i becomes large. These results show that as the axial extent of the blade becomes large with respect to the case radius of the pump, more of the circulation growth occurs within the blade region.

In Figures 3a and 3b the individual contributions to the total induced velocity have been plotted as well as the total value. It can be seen that the effect of another blade and its downstream vorticity is little different than the downstream effect of the "removed" blade. The effects of the mutual blade interference are compared to the effects of the total downstream vorticity by the dotted curves which represent simply the downstream vorticity results multiplied by the number of blades on the impeller. For the two-vaned case given in Figure 3a,

the separate effect of the other blade is seen to be small. It appears, then, that two-vaned impellers with small axial extent might be designed with reasonable success by considering only the downstream vorticity. Neglecting mutual blade interference removes the restriction of the blade angle imposed in the present calculation. When the axial extent is large, or there are several blades, then mutual blade interference should be included.

III. IMPELLER DESIGN METHOD

A. The Streamline Equation

An impeller blade is designed by placing a camber line on the pre-existing streamline in the blade region. The camber line could be put on the streamline at an angle of attack; however, for consideration of improved cavitation conditions it is thought that the best way to achieve the design head is by using camber only rather than by operation at angle of attack. Normally for a cambered blade shape shockless entry occurs approximately at zero angle of attack to the chord line and a smooth pressure distribution is obtained. If the pressure distribution has a large negative area at the leading edge, which is the case with angle of attack, then cavitation is more likely to occur.

The first step is to determine the streamline. Figure 5a shows the relations between the coordinates, the velocity triangle, and elemental streamline triangle. From the triangles it is seen that:*

$$\tan\beta = \frac{dz}{r\,d\theta} = \frac{V_a}{u - V_\theta}$$

where

$$V_\theta = \frac{\Gamma_2}{r_2}\, C_\theta$$

* See Appendix I - - Notation

and C_θ is given by the interference calculation,

$$C_\theta = K_o + K_1 \left(z/z_t \right) . \tag{1}$$

So,

$$V_a \, r \, d\theta = \left[\omega r - \frac{\Gamma_b}{r_2} \left\{ K_o + K_1 \left(z/z_t \right) \right\} \right] dz .$$

Integrating this equation gives,

$$\theta = \frac{\omega z_1}{V_a} - \frac{\Gamma_b}{r_2} \frac{K_o z_1}{r V_a} - \frac{K_1 z_1^2 \Gamma_b}{2 z_t r r_2 V_a} .$$

Dimensionless parameters are introduced:

$$\phi_e = \frac{V_a}{u_2} = \frac{V_a}{\omega r_2} = \frac{Q}{a u_2}$$

where ϕ_e is the design flow rate coefficient;

$$\xi = z/r_2 , \qquad \xi_t = z_t/r_2 ,$$

$$\eta = \frac{r}{r_2} , \qquad \eta_1 = r_1/r_2 ;$$

and the equation above becomes

$$\theta = \frac{\xi}{\phi_e} - \frac{\Gamma_b}{\phi_e r_2^2 \omega \eta} \left[K_o \xi + \frac{K_1 \xi^2}{2 \xi_t} \right] . \tag{2}$$

Equation (2) is the streamline equation, where ϕ_e and $\Gamma_b/\omega r_2^2$ are design constants to be determined. ϕ_e represents the flow rate and Γ_b is related to the pump head.

The blade angles (β_c) the lift coefficients (C_L) and the design head coefficient (ψ_e) will be introduced. The hub blade angle, β_{c_1}, is determined as follows:

$$\tan \beta_{c_1} = \frac{z_{1t}}{r_1 \theta_{1t}} = \frac{\xi_t}{\eta_1 \theta_{1t}}$$

where θ_{1t} is the value of θ at the trailing edge of the root section. Substituting Equation (2) for θ_{1t} (properly evaluated), then

$$\cot \beta_{c_1} = \frac{\eta_1}{\phi_e} - \frac{\Gamma_b}{\phi_e \omega r_2^2} \left[K_{01} + \frac{K_{11}}{2} \right] \qquad (3)$$

where K_{01} and K_{11} are the interference velocity constants at the root section. Lift coefficient is introduced from the equations of airfoil theory:

$$L' = \rho V \Gamma_b = \frac{1}{2} \rho V^2 c C_L$$

where

L' = lift / unit width

ρ = fluid density

c = chord length = $z_t / \sin \beta_c$.

V is approximated by V_R average - - the average relative velocity:

$$V \cong V_R \cong V_a / \sin \beta_c \quad .$$

Solving for Γ_b , dividing through by ωr_2^2, and evaluating

at the root section produces

$$\frac{\Gamma_b}{\omega r_2^2} = \frac{1}{2} \phi_e \xi_t \frac{C_{L_1}}{\sin^2 \beta_{c_1}} \quad . \tag{4}$$

Equations (3) and (4) may be re-solved for ϕ_e and $\Gamma_b/\omega r_2^2$ with the results:

$$\phi_e = \frac{2 \eta_1 \sin \beta_{c_1}}{2 \sin \beta_{c_1} \cos \beta_{c_1} + \xi_t C_{L_1} \left(K_{01} + \frac{K_{11}}{2} \right)} \; ; \tag{5}$$

$$\frac{\Gamma_b}{\omega r_2^2} = \frac{\xi_t \eta_1 C_{L_1}}{2 \sin \beta_{c_1} \cos \beta_{c_1} + \xi_t C_{L_1} \left(K_{01} + \frac{K_{11}}{2} \right)} \; ; \tag{6}$$

and also,

$$\frac{\Gamma_b}{\phi_e \omega r_2^2} = \frac{C_{L_1} \xi_t}{2 \sin^2 \beta_{c_1}} \quad . \tag{7}$$

Equation (2) can be rewritten as:

$$\theta = A \xi - \frac{B}{\eta} \left(K_0 \xi + \frac{K_1 \xi^2}{2 \xi_t} \right) \tag{8}$$

where $A = 1/\phi_e$ and ϕ_e is given by Equation (5) and B is given by Equation (7). A and B are constants determined by the performance desired and depend on the choices of the parameters C_{L_1}, ξ_t, ω, and the number of blades (n). K_0 and K_1 depend upon the number of blades and the axial extent ratio (ξ_t), and are functions of the radius.

B. <u>The Lift Coefficient and Design Head Coefficient</u>

The variation of the amount of the camber (lift coefficient) with radius is determined thus: From airfoil theory

$$C_L = \frac{2\Gamma_b}{V_R C}$$

where $V_R \cong V_a / \sin\beta_c$, $c = z_t / \sin\beta_c$,

and $V_a = \omega r_2 \phi_e$.

Combining these expressions with Equation (7) gives

$$C_L = \frac{C_{L1} \sin^2\beta_c}{\sin^2\beta_{c1}} \quad . \tag{9}$$

The blade angle, β_c , varies with radius as determined from the relation $\tan\beta_c = \xi_t / \eta\theta_t$

Equation (8) gives the value of θ_t . Thus

$$\beta_c = \cot^{-1}\left[A\eta - B\left(K_0 + \frac{K_1}{2}\right)\right] \quad . \tag{10}$$

The head coefficient is found by considering the theoretical head relation for zero prewhirl,

$$H = \frac{u V_{\theta\infty}}{g} \quad .$$

The design head coefficient is defined as:

$$\psi_e = \frac{H g}{u_2^2} \quad ,$$

where all values are taken at the design flow rate. Then

$$\psi_e = \frac{u V_{\theta\infty}}{u_2^2} = \frac{r V_{\theta\infty}}{\omega r_2^2} \quad .$$

But,

$$V_{\theta\infty} = \frac{n\Gamma_b}{2\pi r}$$

is the circulation velocity far downstream.

So, $$\psi_e = \frac{n \Gamma_b}{2 \pi \omega r_2^2} \tag{11}$$

$\Gamma_b/\omega r_2^2$ is given in Equation (7).

C. Calculating Procedure

When all of the performance quantities and parameters have been properly chosen, the streamline constants A and B can be calculated from Equations (5) and (7) and the streamline coordinates can be computed from Equation (8). The values of the blade angle at various radii are calculated from Equation (10), and the variations of C_L are determined from Equation (9). These are the necessary quantities to determine the final blade shape.

Unfortunately, proper choices of the physical parameters cannot be made easily. Usually the desired head and flow rate are specified and they can be expressed by the dimensionless coefficients

$$\psi_e = \frac{H g}{(\omega r_2)^2}$$

and

$$\phi_e = \frac{Q}{\omega \pi r_2^3 (1-\eta_1^2)}$$

However, the choices of ω and r_2 are not independent but must be compatible with the necessary choice of $\beta_{c_1} \cong 32.4^\circ$

and with the choices of n , ξ_t , and C_{L1} . Furthermore, K_{01} and K_{11} depend upon the choice of n and ξ_t . It is almost necessary to use a trial and error method of choosing these quantities to make them satisfy all the Equations (5) through (11).

A guide to the choices is given by the following equations derived by algebraic manipulation of the previous relations with the dimensionless parameters removed.

$$\frac{4\pi^2 g H \sin^2\beta_{c1}\,(1-\eta_1^2)}{Q} = \frac{\xi_t\,\omega\,n\,C_{L1}}{r_2} \quad . \tag{12}$$

given or fixed — to be chosen

$$\frac{Q\cot\beta_{c1}}{\pi\eta_1(1-\eta_1^2)} = \omega r_2^3 - \frac{\pi g H}{\eta_1}\frac{r_2}{n\omega}\left(2K_{01}+K_{11}\right). \tag{13}$$

given or fixed — to be chosen — given or fixed — to be chosen

To proceed with Equations (12) and (13), the given and fixed terms would first be calculated. Secondly a choice of n and ξ_t would be made and consequently K_{01} and K_{11} are determined. Then with a reasonable choice of C_{L1} (say between 0.6 and 1.2), ω and r_2 can be found by solving

Equations (12) and (13) simultaneously. If the speed and size (ω and r_2) are unreasonable, then C_L, can then be changed and new values of ω and r_2 are found. If changes in C_L, over a reasonable range are not sufficient to give plausible speed and size, then a new choice of n and ξ_t should be made and the entire process repeated. Some insight into first choices can be obtained from the example of the test impeller design that is given in Appendix III.

D. Completing the Blade Shape

With the streamline and the lift coefficient determined, the method of completing the blade shape may take alternate forms. The most direct method is simply to plot the streamline and graphically add the camber line to it. Whether the coordinates of the camber (and thickness function) are measured normal to the streamline (and camber line) or normal to the chord line (straight line connecting the end points of the blade) will be of little consequence.

Another method of establishing the blade shape is to consider the streamline "camber" angle as a correction to the isolated airfoil camber angle which gives the required coefficient of lift. The streamline "camber" angle is the difference in the slope of the streamline at the blade leading and trailing edges, $\theta_s = \beta_{s_2} - \beta_{s_1}$.

The isolated airfoil camber angle is the sum of the absolute values of the camber slopes at the leading and trailing edges as given in isolated airfoil data: $\theta_i = \beta_{i1} + \beta_{i2}$ (see Figure 5b). Then the total camber for the blade of an impeller is simply $\theta = \theta_i + \theta_s$. The blade shape with camber angle θ is laid out from the chord line. The geometry and quantities of both of these methods are shown in Figure 5b and demonstrated in Appendix III.

The actual choice of the camber line and thickness function are more dependent upon cavitation conditions than anything else. The object should be to acquire the desired lift coefficient with the least of a minimum static pressure drop. It appears that for this purpose, a symmetrical camber is the best. The thickness function must, of course, have some rounding at the leading edge to keep the blade from being critical to angle of attack, but excessive thickness is not good either as the static pressure drops simply due to the increase in velocity required around a thick leading edge. Any of the standard thickness distributions with "thin" leading edges are probably satisfactory.

For the test impeller, an NACA 85 camber line was employed at the root. This camber line has a lift coefficient of 1.0 (at zero angle of attack) as required by the design procedure. The amount of camber decreased with radius in accord with Equation (9). An NACA 16 - 009

thickness function was added at the hub, and as constant thickness was thought to be most suitable, the percentage thickness was made inversely proportional to the radius.

IV. EXPERIMENTAL PROGRAM

A. Experimental Facilities

The experimental facilities of the rotating channels laboratory of the California Institute of Technology have been described many times in Hydrodynamics Laboratory reports. In the present experiments, the test impeller was operated in a cylindrical case and discharged into an open test basin. A small dynamometer drives the test impeller at a controlled speed - - 210 rpm for the present tests. The flow circuit contains a supply pump which permits operation of the test pump over its complete range of flow rate. The flow rate is controlled by a plug type throttle valve and is measured by any of three venturi meters. Readings are made on mercury manometers.

The test pump consists of the impeller blades mounted on a straight hub running in a straight cylindrical case. The hub is fitted with a hemispherical nose at the inlet. An axial cross section is shown in Figure (6). No inlet or discharge vanes were employed, as it was the purpose of the test to evaluate the impeller vanes without other influences.

B. Construction of the Test Impeller

The angular and axial coordinates of the upper and lower surfaces of the blade were determined by the graphical method outlined in the design procedure for

several radii. The test impeller design quantities are given in Appendix III. These coordinates were used to spot points on brass stock, then by filing and scraping to these points, a master blade shape was created. A mold box was designed and the master blade was attached to a hub segment and placed in the mold box. Plaster molds were made that separated along the leading and trailing edges of the blade. With a relieved hub segment placed in the mold box a blade could be cast into this segment with exact orientation. Blades were cast using a low melting point lead-bismuth alloy, of the trade name "Cerrocast", for ease in accurately reproducing the master blade shape. The blade making technique is illustrated in Figure 7.

C. Experiments Conducted

The performance of the impeller was determined by head and torque measurements for a number of flow rates. The operation of the blades was studied by measuring the static head distributions over their surfaces and by making loss surveys across the impeller passages.

An inlet velocity survey with the blades absent was made to determine the real fluid effects of the hub and case.

D. Instrumentation

The total head was measured as the change be-

tween a total head probe just upstream of the impeller hub and a probe immediately behind the blades. Measurements of the total head were made at five radii. Simple impact tubes were employed and readings were made on an air-water manometer. The exit tube was rotated to find the maximum reading.

The torque was measured by balancing the reaction of the motor case with weights on a pan with a Statham displacement gage and bridge circuit for a null indicator. The total torque was considered as the torque reading less a tare torque value determined by rotating the hub with the blades removed and blank hub segments in place.

The static head distribution on the blades and the loss measurements were taken with the aid of a rotating manometer read with a stroboscopic light. The blade static head taps were made by casting brass tubes into the blades during the manufacturing process and then drilling .020 inch holes normal to the blade surfaces intersecting the tubes. In this manner the signal was lead to the hub center and upwards to the rotating manometer tubes. Several holes were drilled to each brass tube and during operation all holes but one along each tube were plugged with wax. Loss measurements were made by extending impact tubes from the hub. All of the rotating data were referenced against a total head tube at the hub nose and the equations used in calculating the data and forming the dimensionless coefficients are explained in

Appendix IV. The static head taps, can be seen on the cast blade in Figure 7c and the instrumented impeller is shown in Figure 8.

The inlet velocity survey was made by alternately inserting a total head probe and a static head probe into the flow across the passage in the region of the blade leading edge. Both readings were referenced against a total head probe upstream and the two readings were subtracted to permit calculating the velocity coefficient.

E. Estimation of Errors

Error in the total head readings is not greater than one percent except at the lowest flow rates where fluctuation in the impeller performance occurs. The torque measurements displayed some fluctuation due to vibration of the null instrument, but repeated readings indicate that the reported values are accurate to within one and a half percent. Flow rate measurement is quite accurate with less than one-half percent possible error.

The vane static head measurements are generally accurate to about five percent (the least practical reading on the rotating manometer) all though some static head taps gave erroneous readings due to burrs at the holes. Bad taps were usually obvious and their readings were discarded. The losses measured were generally small, such that the percentage error could be large.

The inlet velocity survey results are accurate within one-half percent except in the boundary layer regions where the velocity gradient is large.

V. EXPERIMENTAL RESULTS AND DISCUSSION

The experimental results are reported in terms of dimensionless coefficients as defined in Appendix I (Notation), and the treatment of the data is described in Appendix IV (Data Reduction).

A. Performance

In Figure 9, the head coefficients measured at five radii are presented. The interesting result is that all radial sections produce nearly the same head over a considerable range of flow rate. When deviation begins, the hub, which has the heaviest loading, stalls off first. Then successive radial sections stall, the tip section being the last to stall. A weighted average of the five head curves was taken as the head of the impeller, and the resultant complete characteristic curves are shown in Figure 10. The performance is compared with the predicted values by first considering the inlet velocity profile shown in Figure 11. There it is seen that the axial velocity component is about five to seven percent above the average value over the greater portion of the passage way. Thus in Figure 10 the calculated value of design performance as indicated by the dotted cross is corrected by six percent to give an expected design point indicated by the solid cross. It is seen that the head produced is about four percent lower than the expected

design point where as the "input" head, ψ', is about one to two percent greater. The "input" head, is the head that would be produced if the efficiency were one hundred percent and is found by dividing the torque by the flow rate, τ/ϕ. The "input" head is the one that should correspond to the theory. Thus it is seen that the expected design performance was closely achieved in the experimental test.

The best efficiency point occurs close to the expected design point; however, the shape of the efficiency curve is of special interest. The efficiency drops off rapidly beyond the maximum point although at flow rates from one half the design value up to the design point the efficiency is high. The best efficiency point occurs at a flow rate about four percent below design. Thus the design point is at the high flow rate end of the high efficiency range. This results from considering the design flow rate to be the "shockless" entry flow rate corresponding to zero angle of attack. Operating at small positive angles of attack evidently gives better efficiency. At negative angles of attack the operation is not good.

B. Blade Static Head Distributions - - Cavitation

In Figure 12 the static head (pressure) distribution on the blades of the pump are shown as a function of the flow rate for several radii. At flow rates below the expected design point it can be seen that there are large pressure differences at the leading edges of the blades corresponding to the positive angle of attack. Above the expected design flow rate the angle of attack

is negative and the resultant pressure distributions are "crossed over". Near expected design flow rate the flow streams smoothly onto the blade giving an oval shaped pressure profile. The actual shockless point seems to occur at a flow rate slightly greater than $\phi = 0.284$ which is about four percent less than the expected design point. The correspondence of the correct pressure distribution, and the best efficiency, is excellent. The four percent deviation from the expected design point represents the maximum error in the performance prediction. In Figure 13 the pressure differentials along the blade have been plotted and the smooth entry point is again demonstrated. The theoretical pressure differential is plotted at the expected design flow rate and the agreement is favorable.

The static head distributions (Figure 12) give an indication of incipient cavitation conditions. Theoretically when the static pressure minimum drops to the vapor pressure, cavitation will begin. The minimum static head coefficient for the impeller is plotted as a positive quantity in Figure 14. It can be seen that the best range of flow rate from the consideration of cavitation roughly spans the shockless entry flow rate. Thoma's cavitation coefficient, σ , can be computed from the minimum static pressure coefficient where the relation is simply,

$$\sigma = -C_p/\psi \qquad *$$

* See Appendix IV

σ is also shown in Figure 14.

The cavitation susceptibility is the same at all radii by virtue of the similar pressure distributions for all radii as seen in Figure 12. This is an important result of the proper design of each radial section. In Figure 14, two aspects of cavitation are apparent. The (-) C_p minimum curve shows when the least cavitation susceptibility occurs for the impeller. It occurs at the shockless entry flow rate. However, for flow rates slightly less, the (-) C_p minimum value is not much larger whereas the head produced is greater. Therefore the minimum of the σ cavitation parameter occurs at a lower flow rate. Though σ may be used as a scaling parameter, it is (-) C_p minimum that shows the true cavitation performance of the impeller.

It is also possible to calculate the applied torque from the static head distributions. The method is outlined in Appendix IV and the result is shown in Figure 15 where it is compared with the measured torque. The agreement is quite good over the high efficiency range of operation. Similarly the lift coefficient can be calculated from static head distribution in an approximate manner and the ratio of C_L calculated and the design C_L is given in Figure 16 as a function of radius. This curve demonstrates the correctness of the design procedure with respect to radial sections - - note the radial influence of the inlet velocity profile.

C. Loss Measurements

The loss curves are presented in Figure 17 as a function of the angular distance between the blades for several radii. Over the linear range of the head curves, the losses are not large. The boundary layer at the case is most prominent. The losses may be slightly larger near the suction sides of the blades especially toward the hub where the section loading is greater. At low flow rates and at the highest flow rate gross separations of the flow occur. Unfortunately accurate measurements quite close to the blades were not possible in the present tests, so little was actually learned about real fluid secondary flows. However, from the over-all results, the real fluid effects on the blades are not important considering the correct variation of section loading. Over the high efficiency region, averages of the loss measurements agree reasonably well with the difference between ψ' and ψ .

D. Discussion

The agreement between the theoretical performance predicted by the design procedure and the performance achieved is believed to be good. The best efficiency point, the shockless entry point and best conditions for cavitation all occur at the same flow rate which is about four percent less than the expected design point. The input head is about one to two percent greater that the predicted value at the expected design point. The design method predictions and the experimental results agree then

to within five percent. This discrepancy is not large and maybe due to any number of causes. Further discussion of the present interference theory is reserved for the last section of the text.

Aside from performance prediction, there are certain features of the design procedure that have considerable merit as demonstrated by the experimental results. Two factors are particularly important: the first is the radial variation of the blade chord, and the second is the type of airfoil section used. Their importance lies in the considerations for reduced cavitation susceptibility and in the considerations for off-design performance. Such considerations coupled with the stipulation of free vortex design show that these factors are not determined in a completely arbitrary manner. Free vortex design implies constant angular momentum in the fluid, and consequently constant total head over the radial sections. Also implied is constant circulation, Γ_b , along the blade which requires that the lift (force component perpendicular to the blade chord line) vary radially with the average relative velocity in accordance with the equations of airfoil theory,

$$L' = \rho V_R \Gamma_b = \frac{1}{2} \rho V_R^2 c C_L$$

However, with Γ_b = constant for all radii, and with

$$V_R \cong V_a / \sin \beta_c \quad ,$$

then $L' \sin \beta_c$, the horizontal component of the lift, is also constant for all radii. This requires that the product of the pressure differential and the vertical projection of the blade area be constant. $V_R \, c \, C_L =$ constant at all radii is equivalent.

1. Cavitation Considerations

At one given flow rate (the design point) the above requirements can be met quite easily; in fact c and C_L can have various values within the constant product. In the past designers have made arbitrary choices of c and C_L. Usually the chord did not vary with radius or did not increase sufficiently to give constant axial extent. Therefore the pressure differentials at the outer sections were larger than near the hub. Correspondingly the pressure minimum at the tip was less than at the hub making the tip more susceptible to cavitation. In the present design method cavitation susceptibility has been made equal at all radial sections with the belief that over-all cavitation susceptibility is thereby reduced. Thus the axial extent of the blade is made constant and consequently the variations of the chord and lift coefficient are determined.

2. Off-design Operation

Usually nothing like free vortex operation is achieved at other than the design flow rate. Again the free vortex relationship, $V_R \cdot C_L = \text{constant}$, is considered. As the flow rate changes, V_R changes as a trigonometric function complicated by the interference effects. C_L varies as a function of the absolute angle of attack from the zero lift direction. Both the variance and the zero lift direction depend upon the interference effects and are generally unknown. Therefore meeting the free vortex condition at other than one flow rate is not entirely possible. In the present design procedure an approximation to free vortex operation over the range of flow rate has been accidentally achieved by the radial design considerations for cavitation. This can be explained by considering an approximate stipulation for free vortex operation at all flow rates. The lift is nearly a linear function of angle of attack, so if two flow rates can satisfy free vortex conditions, then the rest of the flow range (before stall) will also. The design point constitutes one such flow rate. The other may be taken as the choke off (zero head) flow rate thus requiring all radial sections to be at zero lift. This requirement is approximately met if the zero lift direction lines of all radial sections drawn through a radial line form a helical surface. Evidently, the present test impeller,

roughly satifies the requirement by virtue of the stipulation of constant axial extent. A further investigation into radial section design might prove beneficial.

The inlet velocity profile has been accounted for in determining an average expected design flow rate as explained in Section A above. However, in Figure 11 it is seen that the velocity decreases from hub to case, especially so near the case. This decrease in velocity is reflected in the static head distribution data and in all other quantities calculated from this data. Thus, the inlet velocity profile explains the radial discrepancy between the experimental results and the design procedure.

For the complete pump a diffusing section must also be considered. The experimental impeller herein described has a reaction of from ninety to ninety-five percent at the design point. This means that only about five to ten percent of the total energy produced by the impeller is recoverable from the tangential velocity component. It seems reasonable then that diffusing blades need not be very large or heavily loaded. In fact considering that diffusion blades in themselves will add losses, perhaps the most efficient diffuser would be no diffuser blades at all. The above premise is, of course, valid only at the design point for at operation at lower flow rates and higher head the reaction is not nearly so high.

VI DISCUSSION OF TURBOMACHINE THEORIES

In Figure 18 the experimental results are compared with the predictions of the present method and of two cascade calculations[5][6] using the geometrical quantities of the test impeller. Each of these results is compared with the result that would be obtained if the radial sections were operated as isolated airfoils. The percentage difference (based on the isolated airfoil) of lift coefficients (heads) are plotted versus radius. The present design method shows the best agreement with the experimental results. Both of the cascade calculations indicate correction in the wrong direction with a total error involved of about twenty-five to thirty percent. As cascade theory is a quite accurate tool for designing axial flow compressors it is somewhat surprising to find such an error in the prediction for pump impeller performance. It is of interest then to determine the cause of this discrepancy.

A. Comparison of Two-Dimensional and Three-Dimensional Theories and Their Applications

The present three-dimensional interference calculation can not be compared directly with cascade theory. There are certain aspects of the methods that have no correspondence. The three-dimensional method, as presented, is approximate, but it is believed to be

based on correct fundamental concepts. Likewise cascade theory is soundly based and is as good as the necessary simplifying assumptions. However, there is one outstanding difference in the results. The three-dimensional method shows that less lift will be obtained from a blade section in an impeller than would be obtained if the section were operated as an isolated airfoil. Cascade theory would give either less or more lift depending on the values of the two-dimensional parameters. These conflicting results indicate that there must be some error in the approximations or assumptions of one or the other or both of the two approaches. Although the experimental evidence is not sufficient to reveal the source of the difficulty, the experimental results strongly favor the approximate three-dimensional procedure.

The geometry of a compressor (where cascade theory is most used) and of a pump impeller can be quite different even though they may have the same solidity. For example, a pump impeller with two or three blades, a low blade angle, and a small aspect ratio (large axial extent) may have solidity equal to that of a compressor row where there are a large number of blades with a high blade angle and with a large aspect ratio. Therefore, the solidity, which is the primary parameter in cascade theory, is replaced in the three-dimensional approach by two parameters, the axial extent ratio (Z_t/r_2) and

the number of blades. This statement assumes the same blade angle (chord angle) for both cases where the blade angle as used here is the complement of the stagger angle common in cascade terminology. It is quite possible that the solidity and blade angle are not the sufficient parameters for determining pump impeller performance.

B. Extension of Cascade Theory

In the event that two-dimensional parameters are sufficient in describing all turbomachine geometries, the use of cascade theory where there are small blade angles must be investigated. Experimental results for cascades properly applied for low blade angle arrays are unavailable. Furthermore, the investigation of thickness in cascade representation is quite limited. It may be that better knowlege of the blade angle parameter and of the effect of thickness will result in more correct cascade formulas for use in designing pump impellers. Shlichting has hinted (Reference 8) that thickness may be a first order quantity with low blade angle cascades. A simple calculation by the author gave the same indication. The thickness effect properly directs the cascade result towards the experimental fact. Hlavka (6) includes thickness in a cascade representation but the effect at low blade angles was not investigated. For further development of theories thickness should be a fundamental consideration.

It may be that cascade results are consistent

but that percentage-wise inherent errors of the cascade method grow large. For compressor design, consideration of the turning angle of the fluid has greater significance in determining performance than does lift coefficient. For the usual pump impellers the fluid turning is quite small and lift coefficient is easier to handle. (Furthermore the lift coefficient is useful in determining blade pressure distribution for cavitation consideration.) An error of small magnitude in the turning angle might be percentage-wise large for a pump.

C. Real Fluid Effects

Neither of the theoretical approaches has considered real fluid effects. Boundary layers can give resultant velocites that are significantly different from those assumed in theories. In fact it was necessary to take the case boundary layer into account in the experimental verification of the design flow rate. With a relative retarding flow, boundary layer growth on a rotating blade may be greater or less than for an isolated airfoil with a consequent difference in operation. Real fluid effects can also be important where low blade angles are used. The boundary layer from one blade may have influence on the operation of the next blade. Thus, the angle of attack of the flow to the blades can be influenced by real fluid action, and where the turning is small, the angle of attack critically affects the performance.

D. Future Design Requirements

The three-dimensional interference calculation and design procedure presented herein has been reasonably successful in the present experimental example. A theory such as is used for cascades wherein the parameters can be varied with simplicity rather than with prolonged numerical calculation would be desirable. Therefore, investigation of the correct use of the parameters listed in section B is worth while.

It is possible, however, to use the present three-dimensional method to design pumps for a variety of performance requirements simply by changing the lift coefficient to give different head coefficients while maintaining the same flow rate coefficient. The specific speed of the experimental example was about 10,000. Thus higher specific speeds can be achieved by reduction of the lift coefficient, or by reducing the axial extent of the vane. A two vaned impeller is sufficient for all specific speeds greater than 10,000. The question of the best ratios of the parameters considering especially cavitation performance arises immediately. Therefore, investigation for designing for optimum cavitation conditions is recommended to complement the present design procedure.

VII CONCLUSIONS

The induced interference calculation has given the following results:

1. The major contribution to the induced tangential velocity is from the total centerline downstream vorticity. When the number of blades is small (three or less) and the axial extent is small ($\xi_t = 0.2$), the downstream vorticity alone is a good approximation for design purposes. When either there are a large number of blades or the axial extent is large, then the mutual effects of the blades must be included.
2. The interference velocity values approach correct limits for zero blades and for an infinite number of blades. Also the trend of the tangential velocities with regard to axial extent is apparently correct.
3. For pump impellers, neither uncorrected isolated airfoil theory nor infinite vane theory can give correct design results.

The design procedure and the experimental results reveal the following:

1. The design procedure allows reasonably correct prediction of performance. Allowing a correction to the design flow rate due to the higher passage velocities as compared to the average velocity, then the head produced is about one to two percent higher than

the predicted value. The maximum efficiency and the shockless entry point, which gives the best cavitation condition, occur at a flow rate about four percent lower than the design.

2. The design flow rate is at the high end of the good efficiency range thus permitting satisfactory operation at flow rates below design point but not above.

3. Cavitation susceptibility has been made equal at all radial sections by virtue of specifying constant axial extent of the blades.

4. Approximate free vortex operation over the linear range of the head curve has been achieved with the present test pump as a result of the consideration in item (3) above. Approximate free vortex operation over the operating range of a pump can be achieved if the pump has true free vortex operation at its design point and also has radial sections designed such that all give zero lift at the same value of choke off flow rate.

5. Pump impellers with high reaction ratios do not require diffusion blades of great extent or with heavy pressure loading.

Analysis of the present theory and cascade theories gives the following:

1. The present design procedure is supported by the

experimental work whereas use of cascade theory for the present test pump would have resulted in error of about twenty-five to thirty percent.

2. There is indication that the two dimensional parameters of cascade theory are not sufficient for describing the usual geometry of pump impellers.

3. If cascade theories are to be extended to properly include pump impeller design, investigations will have to be made regarding low blade angles and considering thickness.

Finally, the performance of the experimental model shows that axial flow pumps of specific speeds down to 10,000 can be designed successfully with only two blades. For higher specific speeds, the lift coefficient or the axial extent of the blades is reduced. Two-bladed designs are quite easily handled by the procedure presented. The question arises, however, as to what is the optimum choice of the physical parameters with regard to cavitation conditions and efficiency. An investigation of optimizing conditions would be a valuable complement to the present design procedure.

REFERENCES

1. Morelli, D. A., and Bowerman, R. D., "Pressure Distribution on the Blade of an Axial Flow Propeller Pump", Trans. ASME, Vol. 75, No. 6, P. 1007, (1953).

2. Tyson, H. N. Jr., "Three-Dimensional Interference Effects of Finite Number of Blades in an Axial Turbomachine", Hdrodynamics Laboratory Report E-19.1, November 1952, California Institute of Technology.

3. O'Brien, M. P., and Folsom, R. G., "The Design of Propeller Pumps and Fans", University of California Publications in Engineering, Vol. 4, No. 1, (1939).

4. Spannhake, W., "Analysis of Modern Propeller-Pump Design", The David W. Taylor Model Basin Report 621, June 1948.

5. Bowen, J. T., Sabersky, R. H., and Rannie, W. D., "Theoretical and Experimental Investigations of Axial Flow Compressors", Report on Research Conducted Under Contract with the Office of Naval Research, California Institute of Technology, Pasadena, (1949).

6. Hlavka, G. E., "An Approximate Theory for Potential Flow Through Cascades of Airfoils", Ph.D Thesis, California Institute of Technology, Pasadena, (1954).

7. Wislicenus, G. F., "Fluid Mechanics of Turbomachinery", McGraw - Hill, (1947).

8. Schlichting, H., "Problems and Results of Investigations on Cascade Flow", Journel of the Aeronautical Sciences, Vol. 21, No. 3, P. 163, (1954).

9. Abbott, I. H., von Doenhoff, A. E. and Stivers, L. S.,Jr. "Summary of Airfoil Data", NACA TR 824, (1945).

APPENDIX I - - NOTATION

a	Annular area of impeller $= \pi (r_2^2 - r_1^2)$
A & B	Constants appearing in streamline equation
C_θ	Dimensionless tangential interference velocity $= \frac{V_\theta r_2}{r_b}$. Given by the linearized equation $C_\theta = K_0 + K_1 \left(\frac{\xi}{\xi_t}\right)$
C_P	Static head coefficient $= \frac{(h_s - H_T)\, g}{u_2^2}$
ΔC_P	Static head differential coefficient
C_L	Lift coefficient
c	Chord
g	Gravitational constant
H	Head of impeller
H_T	Total head in impeller eye
h_s	Local static head
h_t	Local total head
K_o & K_1	Constants in equation for C_θ
L'	Lift force per unit width
N	RPM
n	Number of blades
Q	Flow Rate (cfs)
r	Radial coordinate
r_2	Case radius
r_1	Hub radius
T	Torque
u	Impeller speed $= \omega r$
V	Velocity
V_R	Relative velocity (average)
V_θ	Tangential componant of interference velocity
V_a	Axial velocity (Through-flow)

x	Coordinate along chord line
y	Coordinate perpendicular to chord line
z	Axial coordinate
z_t	Axial coordinate at blade trailing edge
β	Angle from horizontal
β_c	Blade angle (Chord line angle)
Γ_b	Circulation of a blade
Γ	Total circulation value
η	Radius ratio r/r_2
η_h	Hub ratio = 0.6 for this work
η^*	Efficiency
θ	Angular coordinate, also camber angle
ξ	Dimensionless axial coordinate
ξ_t	Axial extent ratio = z_t/r_2
ρ	Fluid density
σ	Cavitation coefficient = $\frac{NPSH}{H} = \frac{-C_p}{\psi}$
τ	Torque coefficient = $T/\rho a u_2^2 r_2$
ϕ	Flow rate coefficient = $V_a/u_2 = Q/a u_2$
ψ	Head coefficient = $\frac{Hg}{u_2^2}$
ψ'	Input head coefficient = τ/ϕ
ψ_ℓ	Head loss coefficient = $\psi' - \psi = \left(H_T + \frac{(\omega r)^2}{2g} - h_t\right)\frac{g}{u_2^2}$
ω	Angular velocity = $2\pi N/60$
NPSH	Net positive suction head
Δ H	Manometer reading

Subscripts

1	Hub radius; also, angle at leading edge
2	Case radius; also, angle at trailing edge
t	Trailing edge
b	Refers to a single blade
s	Streamline quantity
i	Isolated airfoil quantity
∞	Far downstream

APPENDIX II

A. Reproduced Solution of the Three-Dimensional Interference Effects of a Radial Vortex Element.

The following material has been reproduced from Reference 2 by permission of the author, H. N. Tyson, Jr.

THREE-DIMENSIONAL VELOCITY FIELD DUE TO A SINGLE VORTEX FILAMENT IN A CYLINDRICAL ANNULUS

The following section is devoted to the derivation of expressions for the velocity components of the three-dimensional potential field due to a single radial vortex filament of uniform strength located in a cylindrical annulus, as shown in Fig. 1.

Boundary Conditions and Assumptions

The working fluid is assumed to be incompressible, inviscid and irrotational, and the strength of the filament is taken to be constant, so that no vorticity is shed into the flow. With these stipulations, a velocity potential for the flow exists and satisfies Laplace's equation. In cylindrical coordinates this equation becomes

$$\frac{1}{r}\frac{\partial}{\partial r}\left(r\frac{\partial \phi}{\partial r}\right) + \frac{1}{r^2}\frac{\partial^2 \phi}{\partial \theta^2} + \frac{\partial^2 \phi}{\partial x^2} = 0 \qquad (1)$$

where ϕ is the velocity potential.

The inner and outer cylindrical boundaries of the annulus are assumed to be stream surfaces, i.e.,

(a) $$\left.\frac{\partial \phi}{\partial r}\right|_{r=a,b} = 0$$

It is further supposed that the only singularity in the field is a single radial vortex filament located at $x = \theta = 0$, and that there is no net through flow. Then, at a large distance from the filament, the radial and axial disturbance velocities must vanish; or

(b) $$\lim_{|x|\to\infty} \frac{\partial \phi}{\partial x} = 0$$

(c) $$\lim_{|x|\to\infty} \frac{\partial \phi}{\partial r} = 0$$

At plus and minus infinity, the distribution of tangential velocity in the annulus must be such that the requirements of irrotationality are satisfied. Furthermore, the magnitude of the circulation around the hub on either side of the filament must differ by the vortex strength of the filament. To preserve symmetry, the upstream circulation is chosen as $-\Gamma/2$, and the downstream as $+\Gamma/2$, where Γ is taken as the strength of the filament. Thus the tangential velocities at plus and minus infinity are given by the expressions:

(d) $$\lim_{x\to\infty} \frac{1}{r}\frac{\partial \phi}{\partial \theta} = \frac{\Gamma}{4\pi r},$$

$$\lim_{x\to-\infty} \frac{1}{r}\frac{\partial \phi}{\partial \theta} = -\frac{\Gamma}{4\pi r}.$$

Finally, the boundary conditions must specify the singularity. In the axial plane of the filament the tangential velocity satisfies the equations

(e) $$\frac{1}{r}\frac{\partial \phi}{\partial \theta}\Big|_{x=0} = 0 \quad , \qquad 2\pi - \epsilon > \theta > \epsilon \quad ,$$

(f) $$\frac{1}{r}\frac{\partial \phi}{\partial \theta}\Big|_{x=0} = \frac{\Gamma}{4\pi\epsilon} \quad , \qquad -\epsilon \leq \theta \leq \epsilon \, .$$

Condition (f) is obtained from the value of the line integral $\oint \bar{q} \cdot d\bar{s}$ taken about a small rectangle enclosing the filament of length $2r\epsilon$ and width $2(\Delta x)$, as Δx approaches zero (Fig. 2).

Solution

The solution of Laplace's equation for the given boundary conditions and coordinate system is most easily obtained by separating the variables, i.e.,

$$\phi = R(r)\,\Theta(\theta)\,X(x) \tag{2}$$

From Eqs. (1) and (2) the following solutions are obtained:

$$R(r) \sim J_m(\lambda r) + B\,Y_m(\lambda r) = Z_m(\lambda r), \tag{3}$$

$$X(x) \sim e^{\pm \lambda x}, \tag{4}$$

$$\Theta(\theta) \sim \begin{matrix} \sin \\ \cos \end{matrix} m\theta \, , \tag{5}$$

where m, λ are separation constants, and J_m, Y_m are Bessel functions of the first and second kinds, respectively.

Boundary condition (a) requires that $\frac{dR}{dr}\Big|_{r=a,b} = 0$, and this relation leads to the pair of expressions

$$J_m'(\lambda a) + B\, Y_m'(\lambda a) = 0, \tag{6}$$

$$J_m'(\lambda b) + B\, Y_m'(\lambda b) = 0. \tag{7}$$

Equations (6) and (7) may be combined in a form more convenient for numerical work that follows, i.e.,

$$\frac{J_m'(\mu_{nm})}{Y_m'(\mu_{nm})} - \frac{J_m'(\rho\mu_{nm})}{Y_m'(\rho\mu_{nm})} = 0 \tag{8}$$

where $\rho = \frac{b}{a}$. The subscripts m, n, in Eq.(8) indicate that there are an infinite number of solutions possible denoted by n 1, 2, 3, ··· for each value of m 1, 2, 3,···.

Since the flow field is a periodic function of θ, and is antisymmetric about $\theta = 0°$, Eq. (2), by application of (b), (c) and (d), may be written in the form

$$\phi = \frac{\Gamma}{4\pi}\theta + \sum_{m=1}^{\infty} \sin m\theta \sum_{n=1}^{\infty} A_{nm}\, Z_m(\lambda_{nm} r)\, e^{-\lambda_{nm} x}, \quad x>0 \tag{9}$$

and

$$\phi = -\frac{\Gamma}{4\pi}\theta + \sum_{m=1}^{\infty} \sin m\theta \sum_{n=1}^{\infty} A'_{nm}\, Z_m(\lambda_{nm} r)\, e^{\lambda_{nm} x}, \quad x<0 \tag{10}$$

Furthermore, since the flow field must be continuous at x = 0, it follows that $A'_{nm} = -A_{nm}$.

The constants A_{nm} are determined by boundary conditions (e) and (f). By expressing these conditions in a Fourier series,

$$\frac{1}{r}\left.\frac{\partial \phi}{\partial \theta}\right|_{x=0} = \frac{\Gamma}{4\pi r} + \frac{\Gamma}{2\pi r}\sum_{p=1}^{\infty}\frac{\sin p\epsilon}{p\epsilon}\cos p\theta \quad ;$$

and as ϵ approaches zero,

$$\left.\frac{1}{r}\frac{\partial \phi}{\partial \theta}\right|_{x=0} = \frac{\Gamma}{4\pi r} + \frac{\Gamma}{2\pi r}\sum_{p=1}^{\infty}\cos p\theta \quad . \tag{11}$$

Then, from Eqs. (9) and (11),

$$\frac{\Gamma}{2\pi r}\sum_{p=1}^{\infty}\cos p\theta = \frac{1}{r}\sum_{m=1}^{\infty}\cos m\theta \sum_{n=1}^{\infty} A_{nm}\, Z_m(\lambda_{nm} r), \tag{12}$$

and upon identification of p with m, the coefficients of cos m θ may be equated; i.e.,

$$\frac{\Gamma}{2\pi m} = \sum_{n=1}^{\infty} A_{nm}\, Z_m(\lambda_{nm} r) \quad . \tag{13}$$

The orthogonality properties of Bessel functions permit the coefficients A_{nm} to be expressed in the form

$$A_{nm} = \frac{\Gamma}{2\pi m}\,\frac{\int_a^b r\, Z_m(\lambda_{nm} r)\, dr}{\int_a^b r\, Z_m^2(\lambda_{nm} r)\, dr} \tag{14}$$

The denominator of Eq. (14) may be integrated analytically to obtain

$$2\lambda_{nm}^2 \int_a^b r Z_m^2(\lambda_{nm} r)\, dr = (\lambda_{nm}^2 b - m^2) Z_m^2(\lambda_{nm} b) - (\lambda_{nm}^2 a - m^2) Z_m^2(\lambda_{nm} a).$$

If $$\frac{\gamma_{nm}}{2\lambda_{nm}^2} = \int_a^b r Z_m^2(\lambda_{nm} r)\, dr$$

then,

$$A_{nm} = \frac{\Gamma \beta_{nm}}{\pi m \gamma_{nm}} , \qquad (15)$$

where

$$\beta_{nm} = \int_{\mu_{nm}}^{\rho\mu_{nm}} s Z_m(s)\, ds .$$

In terms of dimensionless axial and radial coordinates (ξ, η) the required velocity potential is found to be

$$\Phi = \pm \frac{1}{4\pi}\left(\theta + 4\sum_{m=1}^{\infty} \frac{\sin m\theta}{m} \sum_{n=1}^{\infty} \frac{\beta_{nm}}{\gamma_{nm}} Z_m(\rho\mu_{nm}\eta) e^{\mp \rho\mu_{nm}\xi}\right), \qquad (16)$$

where the upper and lower signs specify the regions $x \geq 0$ and $x \leq 0$, respectively. Expressions for the radial, axial and tangential velocity components may be obtained by differentiation of Eq. (16).

In order to examine the three-dimensional potential field given by Eq. (16), it was necessary to evaluate numerically the coefficients β_{nm} and γ_{nm} since the sum of the double series was not found in closed form.

Inasmuch as both the coefficients and eigenvalues in Eq. (16) depend on the hub ratio, a specific example was worked out for a hub ratio of 0.6.

NOTATION

(For Appendix II A only.)

Symbols

x	Axial coordinate
r	Radial coordinate
θ	Angular coordinate
a	Hub radius
b	Casing radius
ρ	Reciprocal of hub ratio = b/a
ξ	Dimensionless axial coordinate = x/b
η	Dimensionless radial coordinate = r/b
Γ	Circulation of vortex filament (Fig. 1)
ϕ	Velocity potential
Φ	Dimensionless velocity potential = ϕ/Γ
V_θ	Tangential velocity = $\partial\phi/r\partial\theta$
V_x	Axial velocity = $\partial\phi/\partial x$
C_θ	Dimensionless tangential velocity = $\frac{V_\theta b}{\Gamma}$
C_ξ	Dimensionless axial velocity = $\frac{V_x b}{\Gamma}$
C_η	Dimensionless radial velocity = $\frac{V_r b}{\Gamma}$
n, m	Integers
A_{nm}, B_{nm}	Constants
λ_{nm}	Eigenvalue
J_m	Bessel function of the 1st kind

Y_m	Bessel function of the 2nd kind
Z_{nm}	$J_m + B_{nm}\ Y_m$
ϵ	Infinitesimal angle
μ_{nm}	Dimensionless Eigenvalue = $\lambda_{nm}\, a$
β_{nm}, γ_{nm}	Defined constants

FIGURES

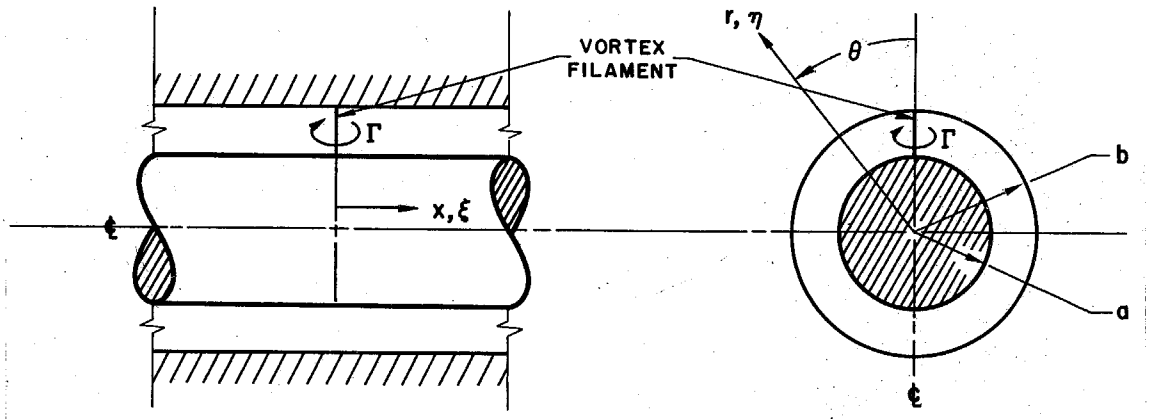

Fig. 1 - Definition sketch of coordinate system.

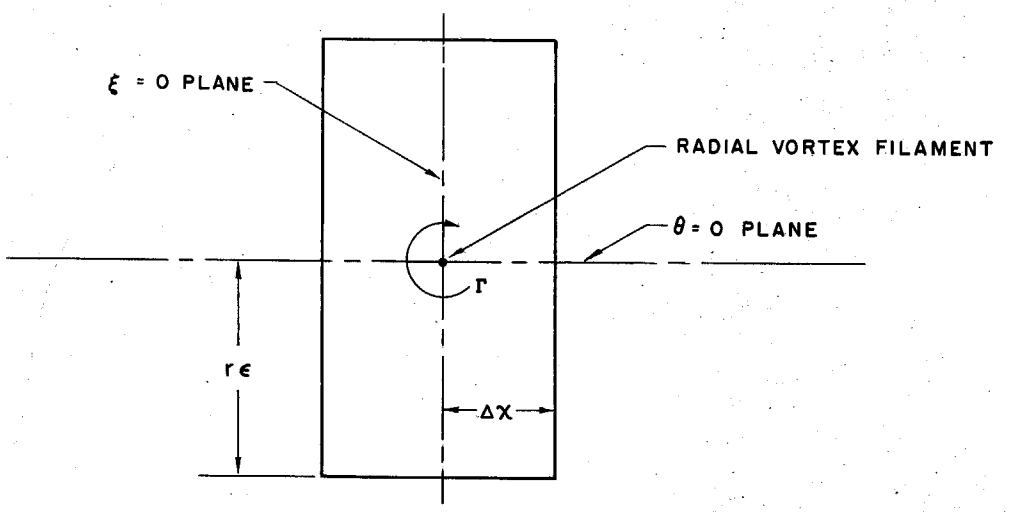

Fig. 2 - Sketch for determination of boundary condition.

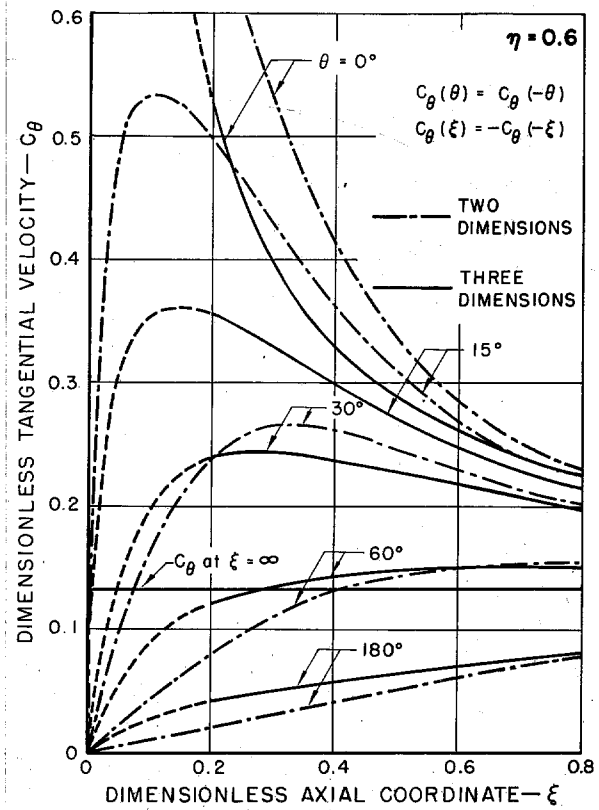

Fig. 4.

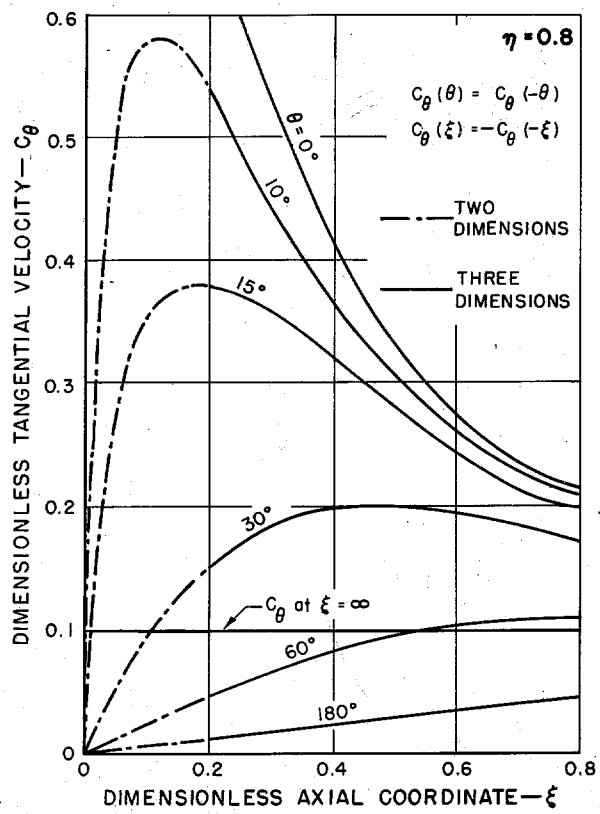

Fig. 5.

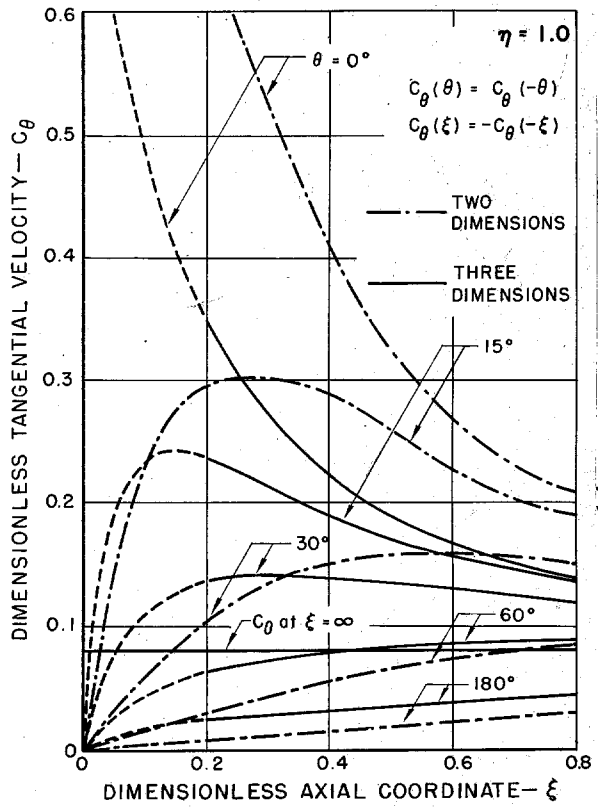

Fig. 6.

Comparison of the two- and three-dimensional tangential velocity distributions at the hub, mean radius and casing. Hub ratio = 0.6.

TABLE I

Three-Dimensional Tangential Velocity Components (C_θ)

		Casing Radii from Filament ($\xi \geq 0$)				
η	θ	0	6/30	10/30	16/30	24/30
0.6	0°		.531	.371	.279	.222
	15	0	.357	.320	.262	.215
	30	0	.240	.243	.224	.197
	45	0	.170	.180	.183	.174
	60	0	.120	.136	.148	.152
	75	0	.091	.106	.122	.132
	90	0	.073	.087	.103	.117
	105	0	.062	.074	.089	.104
	120	0	.054	.065	.080	.095
	135	0	.049	.060	.073	.089
	150	0	.046	.056	.069	.084
	165	0	.044	.054	.067	.082
	180	0	.044	.053	.066	.081
0.8	0°		.800	.484	.308	.214
	15	0	.379	.346	.268	.201
	30	0	.151	.192	.195	.172
	45	0	.078	.112	.136	.140
	60	0	.047	.073	.098	.112
	75	0	.033	.052	.074	.091
	90	0	.025	.040	.058	.076
	105	0	.020	.032	.048	.066
	120	0	.017	.027	.042	.058
	135	0	.015	.024	.037	.052
	150	0	.013	.022	.034	.049
	165	0	.013	.021	.033	.047
	180	0	.013	.021	.032	.046
1.0	0°		.348	.254	.183	.139
	15	0	.236	.205	.166	.134
	30	0	.137	.141	.134	.120
	45	0	.090	.100	.106	.104
	60	0	.065	.076	.085	.090
	75	0	.051	.060	.070	.078
	90	0	.042	.050	.060	.068
	105	0	.036	.043	.052	.061
	120	0	.032	.038	.047	.056
	135	0	.029	.035	.043	.052
	150	0	.027	.033	.041	.050
	165	0	.026	.032	.039	.049
	180	0	.026	.031	.039	.048

B. Flow Field Due to the Downstream Vorticity of a Pump Impeller Blade

The centerline vorticity is assumed to grow linearly from the impeller blade leading edge to the trailing edge with a constant value of circulation Γ_b continuing to infinity.

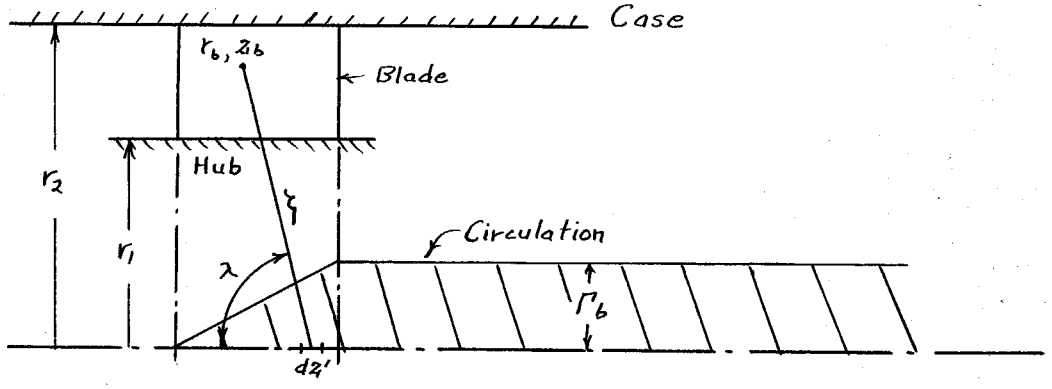

$V_{\theta b}$ is found by combining the equation for a true semi-infinite vortex giving V^I with the equation for the complement of the growth of circulation Γ_b' from $z = o$ to $z = z_t$ which gives V^{II}.

Thus, $$V_{\theta b} = V^I - V^{II}$$

where $$V^I = \int_o^\infty \frac{\Gamma_b}{4\pi} \frac{\sin\lambda}{\zeta^2} dz'$$

and $$V^{II} = \int_o^{z_t} \frac{\Gamma_b'}{4\pi} \frac{\sin\lambda}{\zeta^2} dz' \quad ; \quad \Gamma_b' = \left(\frac{z_t - z}{z_t}\right)\Gamma_b .$$

Also,

$$\sin\lambda = \frac{r_b}{\zeta}\,, \qquad \zeta = \sqrt{z'^2 + r_b^2}\,,$$

$$z' = z - z_b\,.$$

z_b and r_b are the coordinates of the calculating region fixed for the determination of $V_{\theta b}$,

For V^I,

$$V^I = \frac{\Gamma_b r_b}{4\pi} \int_0^{\infty} \frac{d(z - z_b)}{\left[(z - z_b)^2 + r_b^2\right]^{3/2}}\,.$$

Integrating and evaluating the limits of integration gives,

$$V^I = \frac{\Gamma_b}{4\pi r_b}\left[1 + \frac{z_b/r_b}{\sqrt{(z_b/r_b)^2 + 1}}\right]\,.$$

V^{II} is determined as follows:

$$V^{II} = \frac{\Gamma_b r_b}{4\pi z_t} \int_0^{z_t} \frac{(z_t - z)\, d(z - z_b)}{\left[(z - z_b)^2 + r_b^2\right]^{3/2}} = \frac{\Gamma_b r_b}{4\pi z_t} \int_0^{z_t} \frac{\left[(z_t - z_b) - (z - z_b)\right]}{\left[(z - z_b)^2 + r_b^2\right]^{3/2}}\, d(z - z_b),$$

$$V^{II} = \frac{\Gamma_b r_b}{4\pi z_t}\left[\int_0^{z_t} \frac{(z_t - z_b)\, d(z - z_b)}{\left[(z_t - z_b)^2 + r_b^2\right]^{3/2}} - \int_0^{z_t} \frac{(z - z_b)\, d(z - z_b)}{\left[(z_t - z_b)^2 + r_b^2\right]^{3/2}}\right]\,.$$

Performing the integration, evaluation, and grouping of terms gives:

$$V^{II} = \frac{\Gamma_b}{4\pi r_b}\left\{\frac{r_b}{z_t}\left[\sqrt{\left(\frac{z_t - z_b}{r_b}\right)^2 + 1} - \frac{1 - \frac{z_b}{r_b}\left(\frac{z_t - z_b}{r_b}\right)}{\sqrt{(z_b/r_b)^2 + 1}}\right]\right\}\,.$$

Subtracting V^{II} from V^{I} and introducing the dimensionless coefficients,

$$\eta = \frac{r_b}{r_2} \quad , \quad \xi = \frac{z_b}{r_2} \quad , \quad \xi_t = \frac{z_t}{r_2} \quad ,$$

then the equation for $V_{\theta b}$ becomes:

$$V_{\theta b} = \frac{\Gamma_b}{4\pi \eta r_2} \left[1 + \frac{1}{\xi_t} \left(\sqrt{\xi^2 + \eta^2} - \sqrt{(\xi_t - \xi)^2 + \eta^2} \right) \right] .$$

APPENDIX III

Example of the Design Procedure - - The Test Impeller

1. Calculation of Performance Coefficients and the Streamline

The test impeller was designed in an arbitrary manner, but to illustrate the method for choosing the parameters, the calculation shown here proceeds from specified quantities.

Requirements: Head = 12.9 ft

Flow rate = 1590 gpm = 3.54 cfs

Arrange to have N = 1750 RPM.

Fixed: $\beta_{c_1} = 32.4^\circ$, $\eta_1 = 0.6$

(For the testing speed of 210 RPM the above requirements are reduced to H 0.185 ft and Q 0.425cfs) Substituting these values into Equations (12) and (13) gives

$$850 = \frac{\xi_t \omega n C_{u_1}}{r_2},$$

and

$$4.63 = \omega r_2^3 - 2023 \frac{r_2}{n\omega}\left(2K_{01} + K_{11}\right).$$

Choose $n = 2$, $\xi_t = 0.72$,

then $K_{01} = .117$, $K_{11} = .295$. *

* These values are slightly different than those reported in Figure 4. A linearized form of the equation derived in Appendix IIB was used to design the test pump, but as this linear equation does not offer any saving in calculating time it was not used in the final reporting of interference velocities.

Then, $850 = 1.44\ C_{L_1}\ \frac{\omega}{r_2}$,

and $4.63 = \omega r_2^3 - 535\ \frac{r_2}{\omega}$.

The value of C_{L_1} is chosen as 1.0; then ω and r_2 can be determined by solving the above equations simultaneously with the result:

$$r_2 = .312 \text{ ft} = 3.75 \text{ in}$$

$$\omega = 184 \text{ sec}^{-1}\ ,\ N = \frac{60\omega}{2\pi} = 1750 \text{ RPM.}$$

Therefore, the final choices are: $n = 2$, $\xi_t = 0.72$, $C_{L_1} = 1.0$, $N = 1750$, and $r_2 = 3.75$ in.

The design head and flow rate coefficients can be computed. ϕ_e is determined from Equation (5) or more simply by

$$\phi_e = \frac{Q}{a\,\omega r_2} = 0.315 .$$

$$\psi_e = \frac{H\,g}{u_2^2} = 0.126 .$$

The streamline coordinates are calculated from Equation (8) in the following manner. Values of K_0 and K_1 for various radial sections are obtained. B is computed from Equation (7) (A is known from ϕ_e), and for each radial section (η) values of θ are determined for various values of ξ . The blade angles and the values of lift coefficient for the radial sections are calculated from Equations (9) and (10).

2. Completing the Blade Shape

Graphical Method

The chord line and streamline are drawn for each radial section. The camber line coordinates are obtained from NACA data[9] and are linearly scaled to give the proper C_L for each section. The camber line ordinates

are then measured from the streamline. The thickness function is added in the usual manner.

Correction Method

The correction method is not as accurate as the direct graphical method, but gives essentially the same result for symmetrical parabolic camber lines. The "camber" angles of the streamline and camber line are found as follows: For the streamline, the derivative of the streamline equation is found and multiplied by r with the result

$$\cot \beta_s = \frac{r\, d\theta}{dz} = A\eta - BK_0 - BK_1\xi.$$

This equation is evaluated at the leading edge ($\xi = o$) and at the trailing edge ($\xi = \xi_t$) giving β_{s_1} and β_{s_2}. The difference is the streamline camber,

$$\theta_s = \beta_{s_2} - \beta_{s_1}$$

The camber angle of the camberline is found in a similar manner using NACA data to determine the angles β_{i_2} and β_{i_1}. (Note in Figure 5b that the angles β_{i_1} and β_{i_2} are measured from the chord line.) Then $\theta_i = \beta_{i_1} + \beta_{i_2}$. The total camber angle of each blade section is $\theta = \theta_s + \theta_i$. For the test pump, $\theta_{s_1} = 6.15$ degrees and $\theta_i = 35.56$ degrees at the root section, and so $\theta = 41.71$ degrees. The blade camber is then corrected by multiplying the NACA data by the ratio of θ/θ_i and the ordinates are plotted from the chord line in the usual manner.

APPENDIX IV

Data Reduction

1. Dimensionless Coefficients

All head data are made dimensionless by dividing by u_2^2/g,

$$\psi \text{ or } C_p = \frac{(Head)\,g}{u_2^2}.$$

For 210 RPM,

Head (ft) $\quad 1.468\ (\psi \text{ or } C_p)$.

The flow rate coefficient is

$$\phi = \frac{Q}{a\,u_2} = \frac{Va}{u_2}.$$

For 210 RPM,

Q (cfs) $\quad 1.350\,\phi$

2. Static Head Measurements in Rotating Coordinates

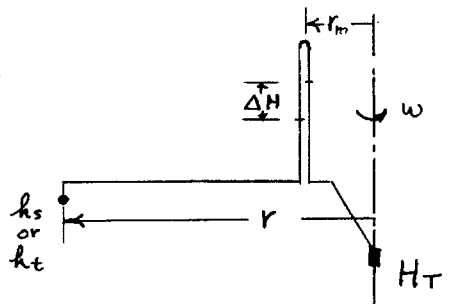

From the schematic diagram it can be seen that for a static tap,

$$h_s - \frac{(\omega r)^2}{2g} + \frac{(\omega r_m)^2}{2g} + \Delta H = H_T + \frac{(\omega r_m)^2}{2g},$$

or

$$h_s - H_T = \frac{(\omega r)^2}{2g} - \Delta H$$

The static head coefficient is defined as:

$$C_P = \frac{(h_s - H_T)}{u_2^2} g \quad .$$

So,

$$C_P = \frac{1}{2}\eta^2 - \frac{\Delta H\, g}{u_2^2} \quad .$$

The static head coefficient is determined by graphically subtracting the manometer reading (made dimensionless) from the line $\eta^2/2$.

For a relative total head tube (see above diagram), then

$$h_t - H_T = \frac{(\omega r)^2}{2g} - \Delta H \quad .$$

However, the Bernoulli Equation (with losses permitted) in rotating coordinates is:

$$\text{losses} + h_t = H_T + \frac{(\omega r)^2}{2g} \quad .$$

Therefore ΔH is the head loss, so the loss coefficient is given as:

$$\psi_\ell = \frac{\Delta H\, g}{u_2^2} = \left[H_T + \frac{(\omega r)^2}{2g} - h_t\right] \frac{g}{u_2^2} \quad .$$

3. Cavitation Coefficients

Ideally, when the minimum value of the static head on the blade surface reaches the vapor pressure (head) then cavitation will begin. Since H_T is the total head at the impeller inlet corresponding to reservoir level, then $H_T - h_s$ is the net positive suction head for incipient cavitation, and

$$-C_{P\,minimum} = \frac{NPSH}{u_2^2}\, g$$

The cavitation coefficient, $\sigma = \frac{NPSH}{H}$, is then, $\sigma = \frac{-C_P}{\psi}$.

4. Calculation of Torque Coefficient from Static Head Distributions.

The torque can be determined by integrating the pressure differentials over the blade surface,

$$T = \iint r \Delta P \, dz \, dr,$$

where $\Delta P = \Delta H \rho g = \rho u_2^2 \Delta C_P$

Then, $T = \rho u_2^2 \iint r \Delta C_P \, dz \, dr.$

The torque coefficient is defined as:

$$\tau = \frac{T}{\rho a u_2^2 r_2}.$$

So,

$$\tau = \frac{1}{a r_2} \iint r \Delta C_P \, dz \, dr.$$

The calculation is carried out by determining the area of the ΔC_P vs. Z curves for various radial sections which gives

$\int \Delta C_p \, dz$. These results are multiplied by the corresponding radius, r, and the values are plotted versus r from r_1 to r_2. The area of this plot is determined giving

$$\iint r \, \Delta C_p \, dz \, dr.$$

5. Calculation of C_L from Static Head Distributions

From airfoil theory,

$$L' = \tfrac{1}{2} \rho V_R^2 c \, C_L = \int_{LE}^{TE} \Delta P \, dc.$$

As before, $\Delta P = \Delta C_P \, \rho u_2^2$,

and so $$C_L = \frac{2u_2^2}{V_R^2} \int_0^1 \Delta C_P \, d(x/c).$$

At the design point V_R has been approximated by $V_R \cong V_a / \sin \beta_c$

and as $V_a / u_2 = \phi_e$,

then $$C_L \cong \frac{2 \sin^2 \beta_c}{\phi_e^2} \int_0^1 \Delta C_P \, d(x/c).$$

The values were calculated for the test pump by finding the area, $\int_0^1 \Delta C_P \, d(x/c)$, for the flow rate six percent less than ϕ_e corresponding to the inlet boundary layer influence. Thus, C_L as determined is quite approximate; however, the radial trend should be reasonably accurate.

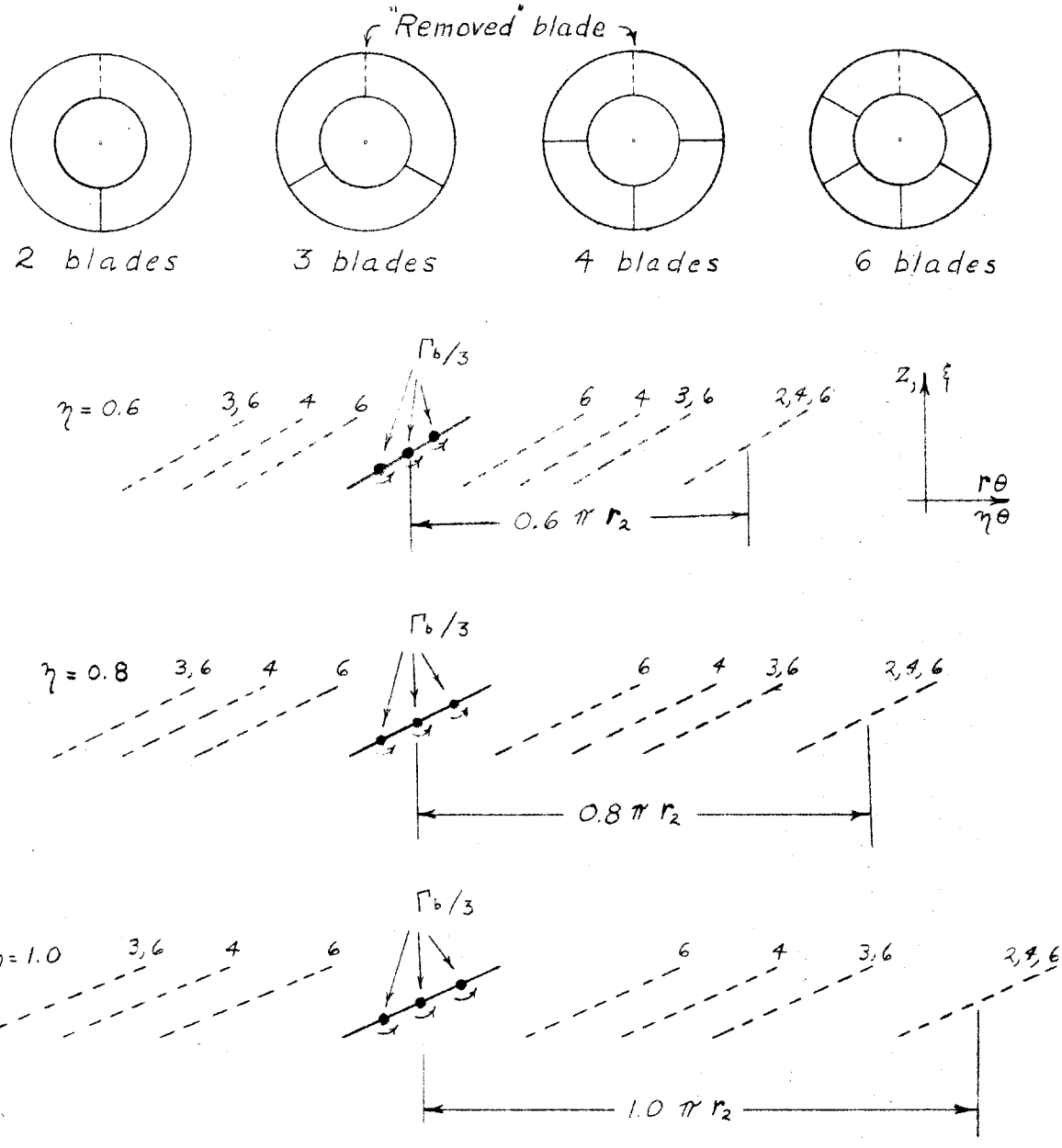

Blade represented by three vortices with $\zeta_t = 0.4$

Three radial sections are shown.

The dotted lines show the summation regions and the numbers above correspond to the number of blades on the impeller.

Figure 1 - Blade representation for summation of mutual interference velocities.

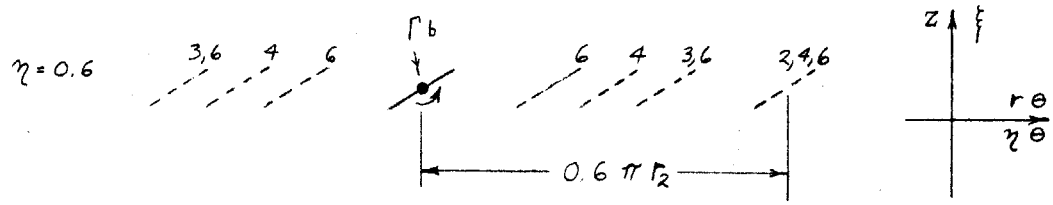

Blade represented by single vortex with $\xi_t = 0.2$

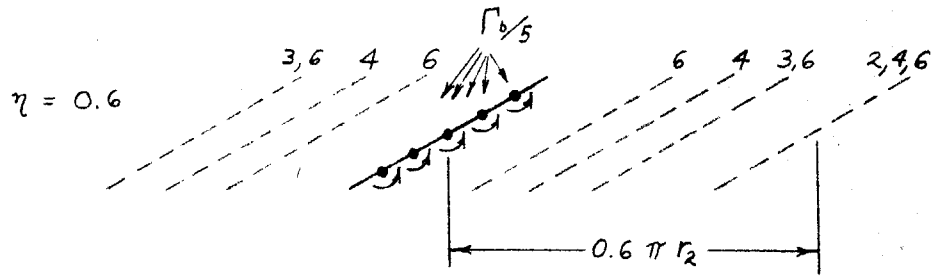

Blade represented by five vortices with $\xi_t = 0.6$

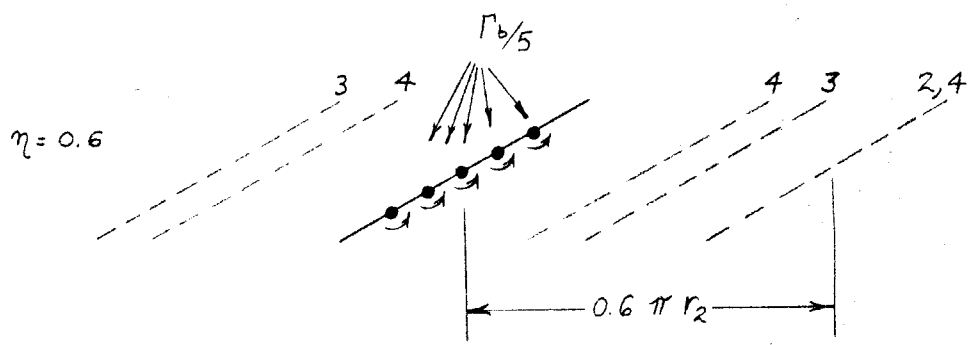

Blade represented by five vortices with $\xi_t = 0.72$

Figure 1 (concluded) - Blade representation for summation of mutual interference velocities.

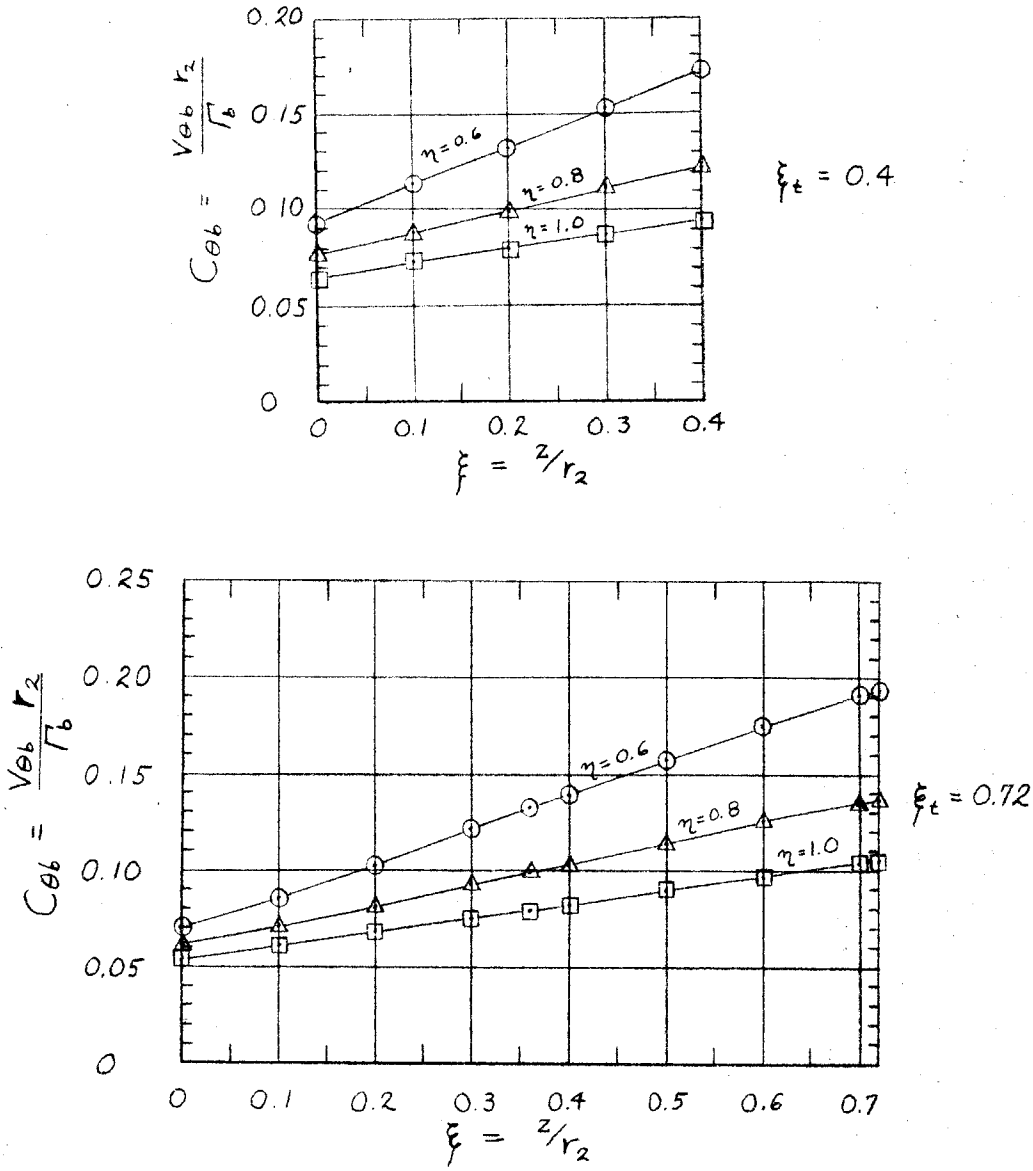

Dimensionless Tangential Velocity vs. Dimensionless Axial Coordinate

Figure 2 - Induced tangential velocity due to the downstream vorticity of "removed" blade for $\xi_t = 0.4$ and for $\xi_t = 0.72$

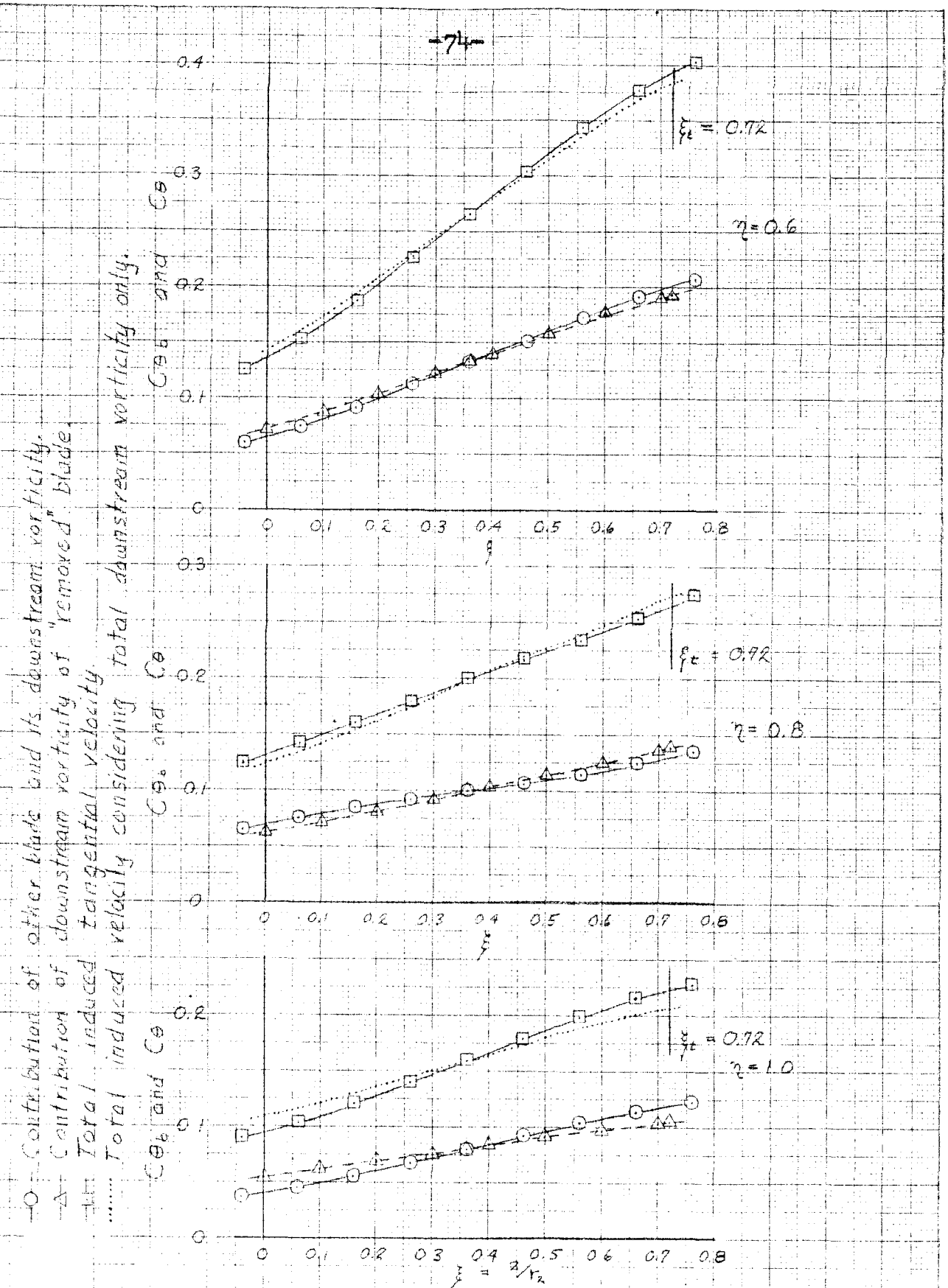

Figure 3a - Tangential induced velocities as a function of the axial coordinate for a two-bladed impeller with $\xi_t = 0.72$

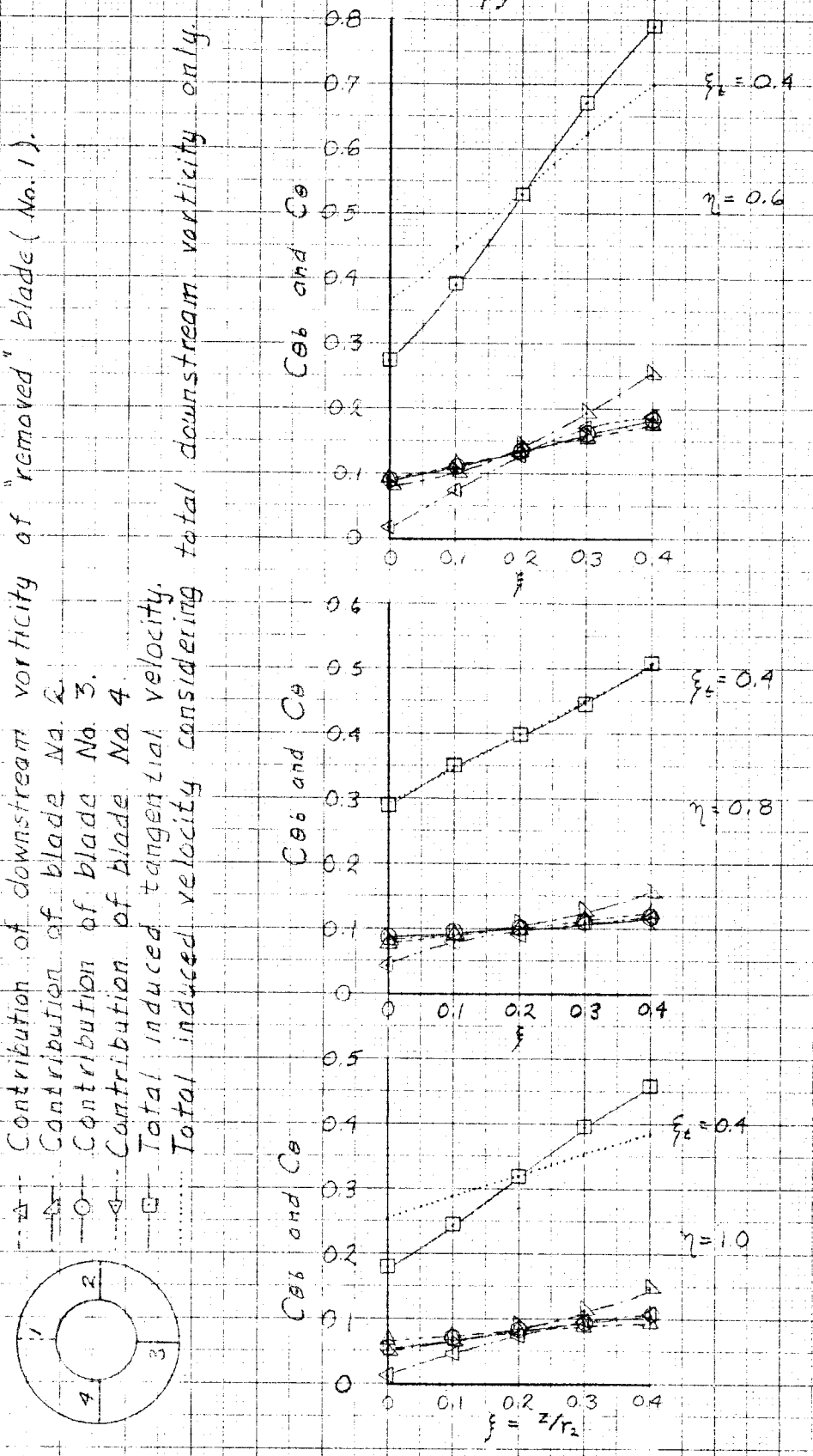

Figure 3b - Tangential induced velocities as a function of the axial coordinate for a four-bladed impeller with $\xi_t = 0.4$.

AXIAL EXTENT	NUMBER OF BLADES	K_0				K_1		
		$\eta = 0.6$	$\eta = 0.8$	$\eta = 1.0$		$\eta = 0.6$	$\eta = 0.8$	$\eta = 1.0$
$\xi_t = 0.2$	2	0.212	0.180	0.134		0.106	0.038	0.051
	3	0.299	0.269	0.186		0.198	0.059	0.105
	4	0.371	0.352	0.231		0.319	0.092	0.174
	6	0.463	0.501	0.304		0.665	0.192	0.348
$\xi_t = 0.4$	2	0.180	0.161	0.118		0.170	0.076	0.083
	3	0.241	0.235	0.156		0.315	0.128	0.159
	4	0.274	0.288	0.180		0.514	0.220	0.277
	6	0.289	0.310	0.191		1.015	0.574	0.574
$\xi_t = 0.6$	2	0.152	0.142	0.103		0.227	0.114	0.112
	3	0.183	0.187	0.125		0.430	0.224	0.228
	4	0.187	0.191	0.128		0.687	0.415	0.381
	6	0.191	0.184	0.127		1.210	0.826	0.701
$\xi_t = 0.72$	2	0.135	0.130	0.093		0.258	0.137	0.129
	3	0.149	0.159	0.103		0.493	0.280	0.268
	4	0.138	0.144	0.100		0.781	0.505	0.433

Figure 4a - Table of values of K_0 and K_1 describing the total induced tangential velocity.

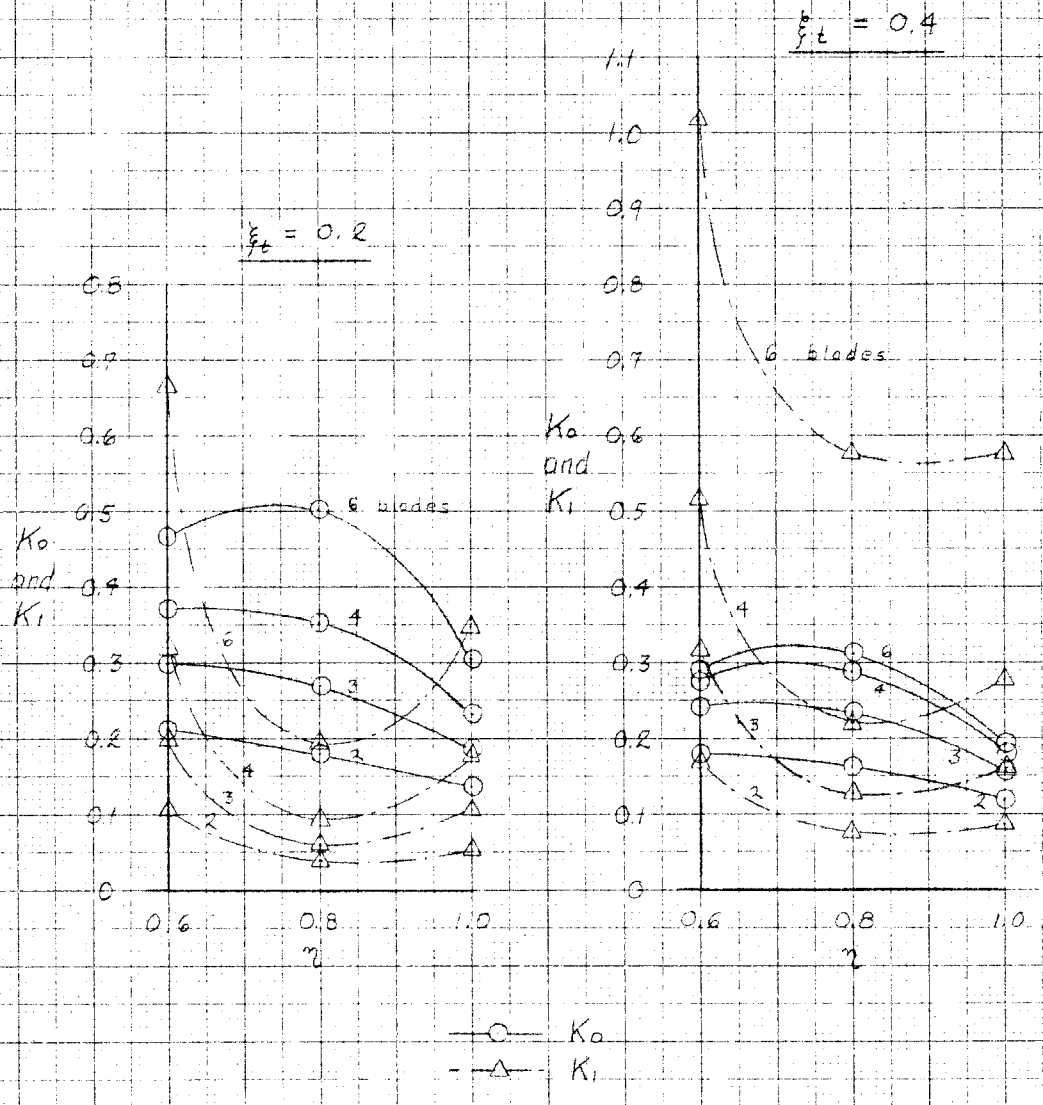

Figure 4b - K_0 and K_1 shown as a function of the radius ratio for several numbers of blades.

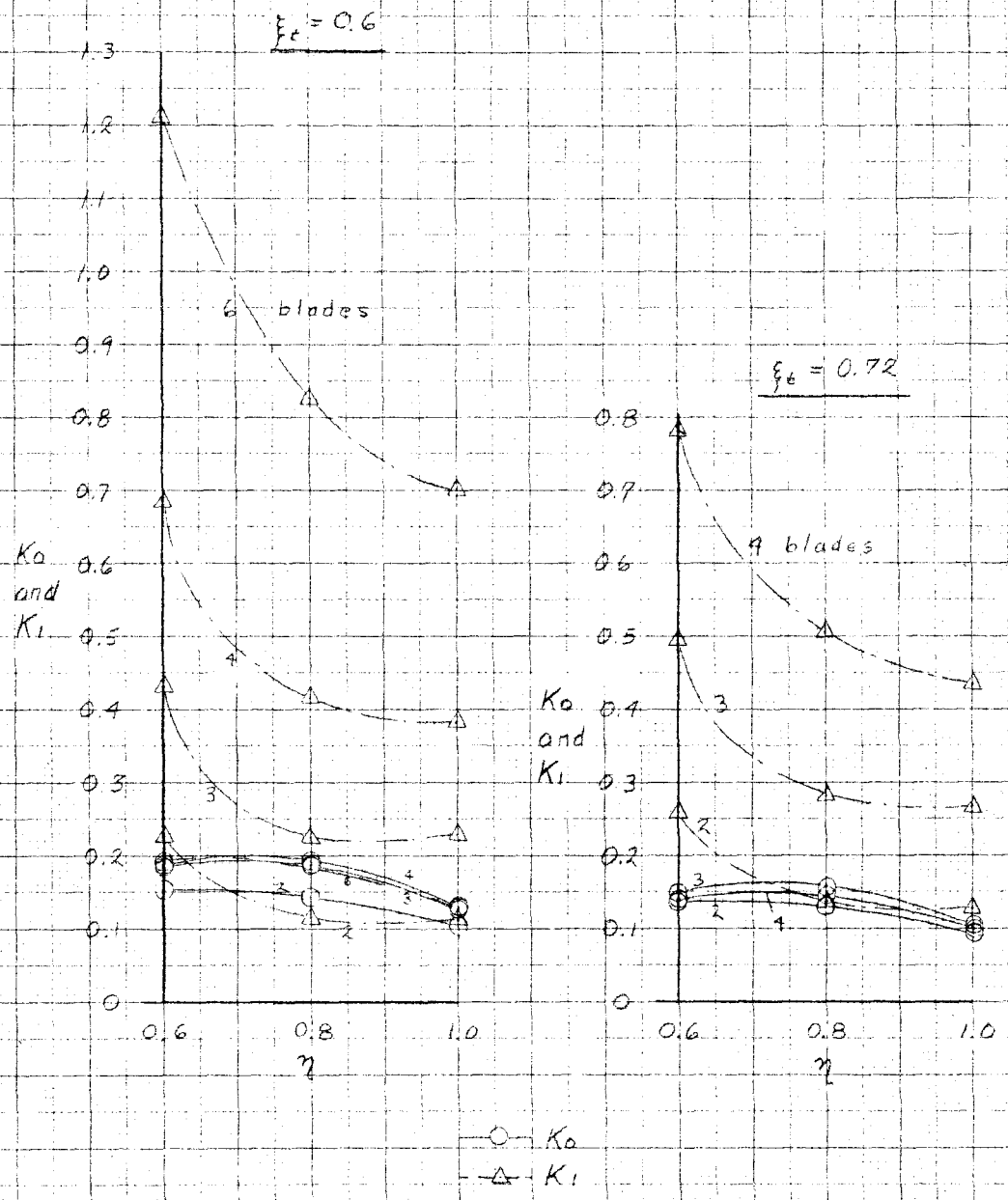

Figure 4b (concluded) - K_0 and K_1 shown as a function of the radius ratio for several numbers of blades.

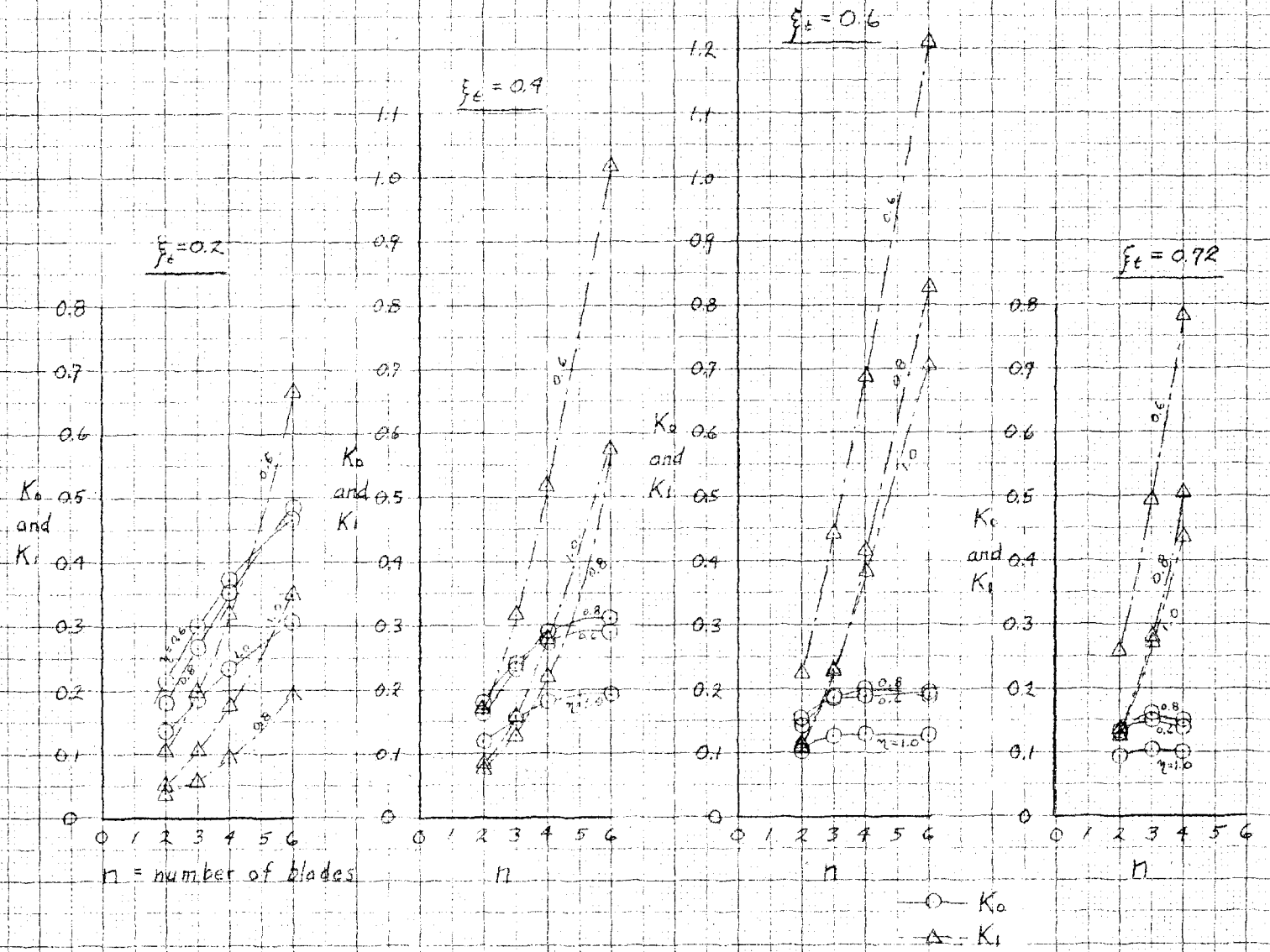

Figure 4c - K_0 and K_1 shown as a function of number of blades.

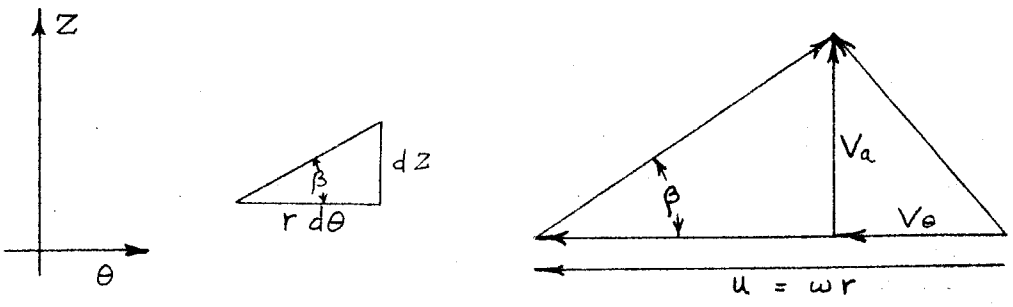

Figure 5a - Velocity components and the coordinate system.

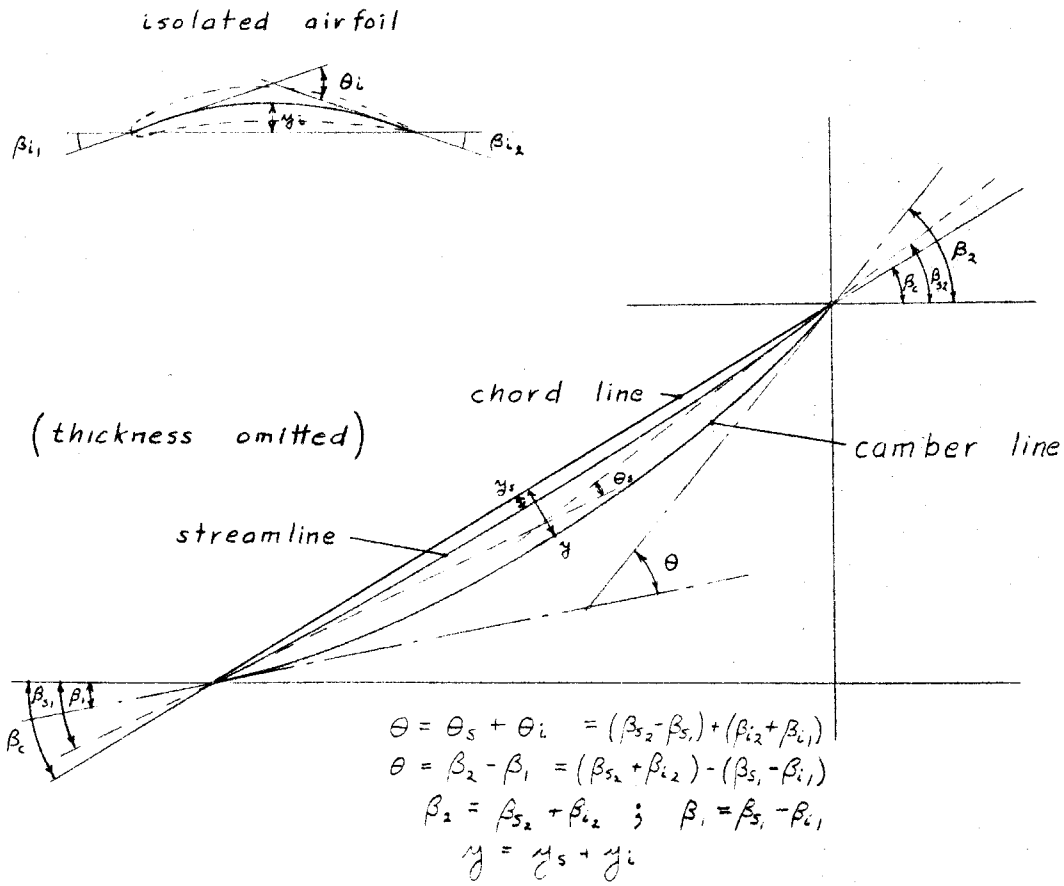

Figure 5b - Geometry of blade section.

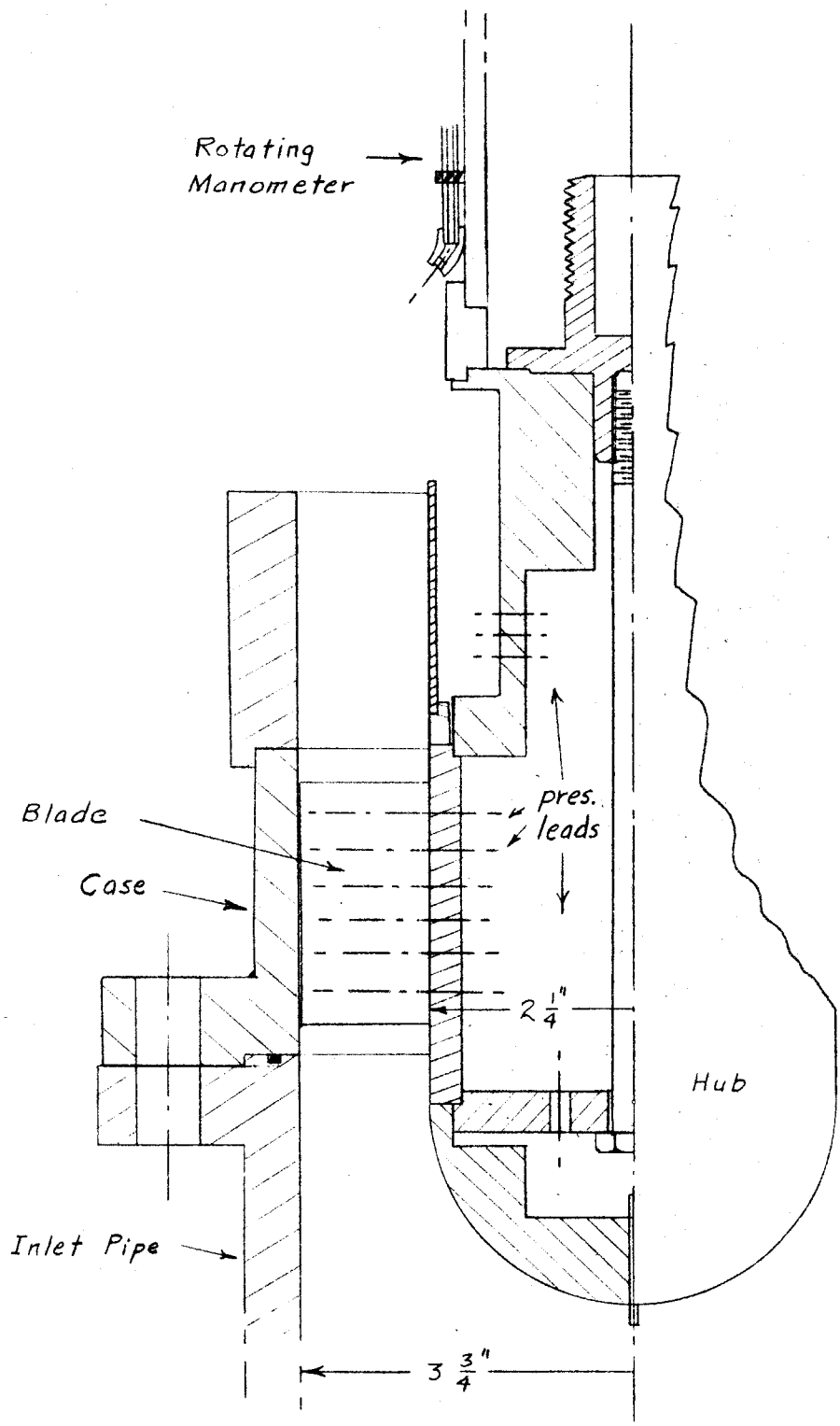

Figure 6 - Axial cross section of test pump.

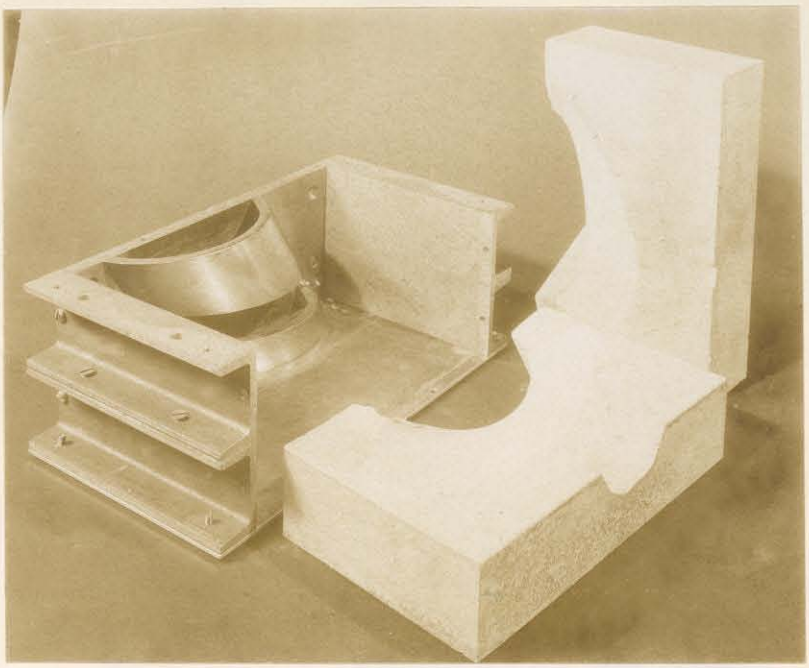

Figure 7a - Mold box with slotted hub piece and plaster mold halves.

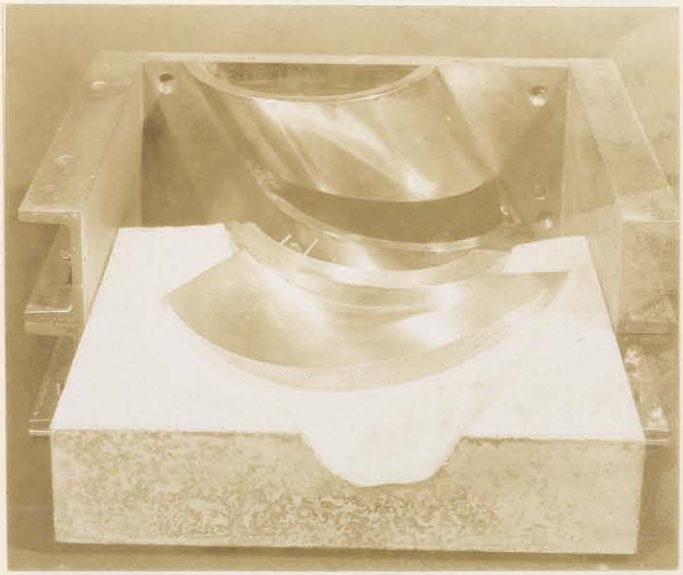

Figure 7b - Blade cast onto hub segment that fits into slot of hub piece in mold box and into impeller hub thus insuring correct orientation.

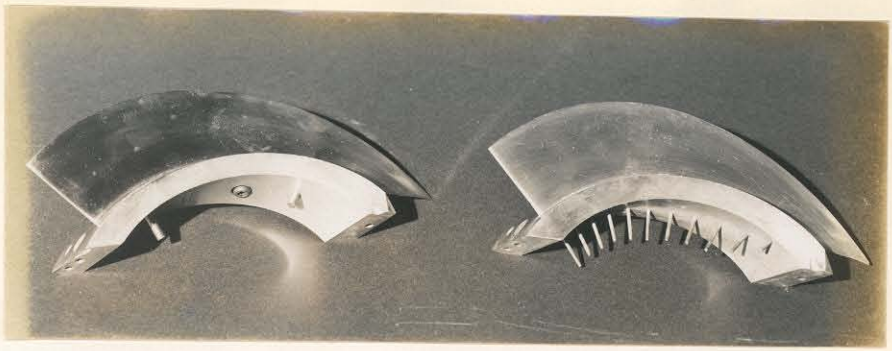

Figure 7c - Brass master blade on left and reproduction on right.

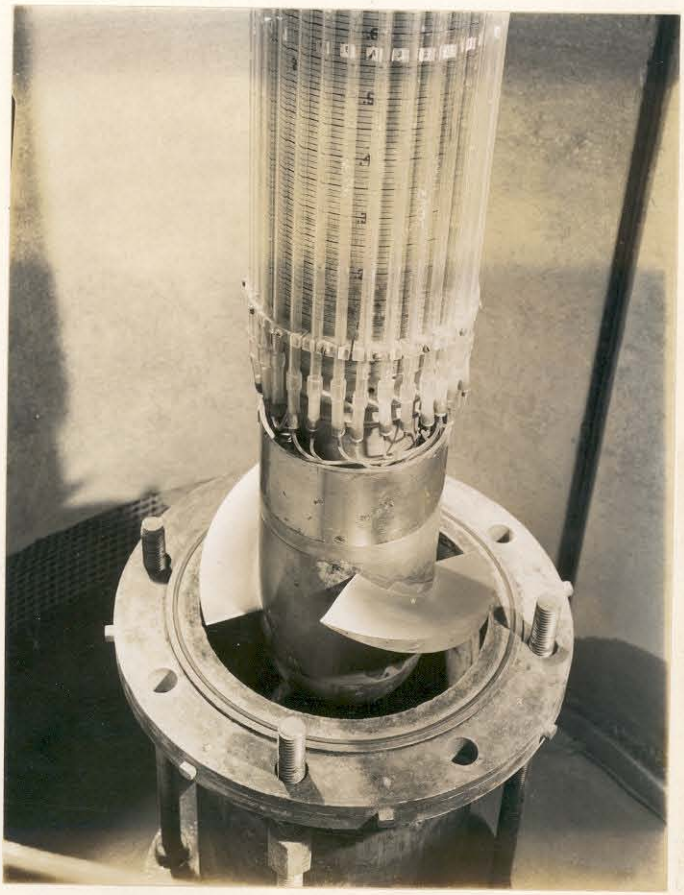

Figure 8 - Impeller and rotating manometer with the case removed.

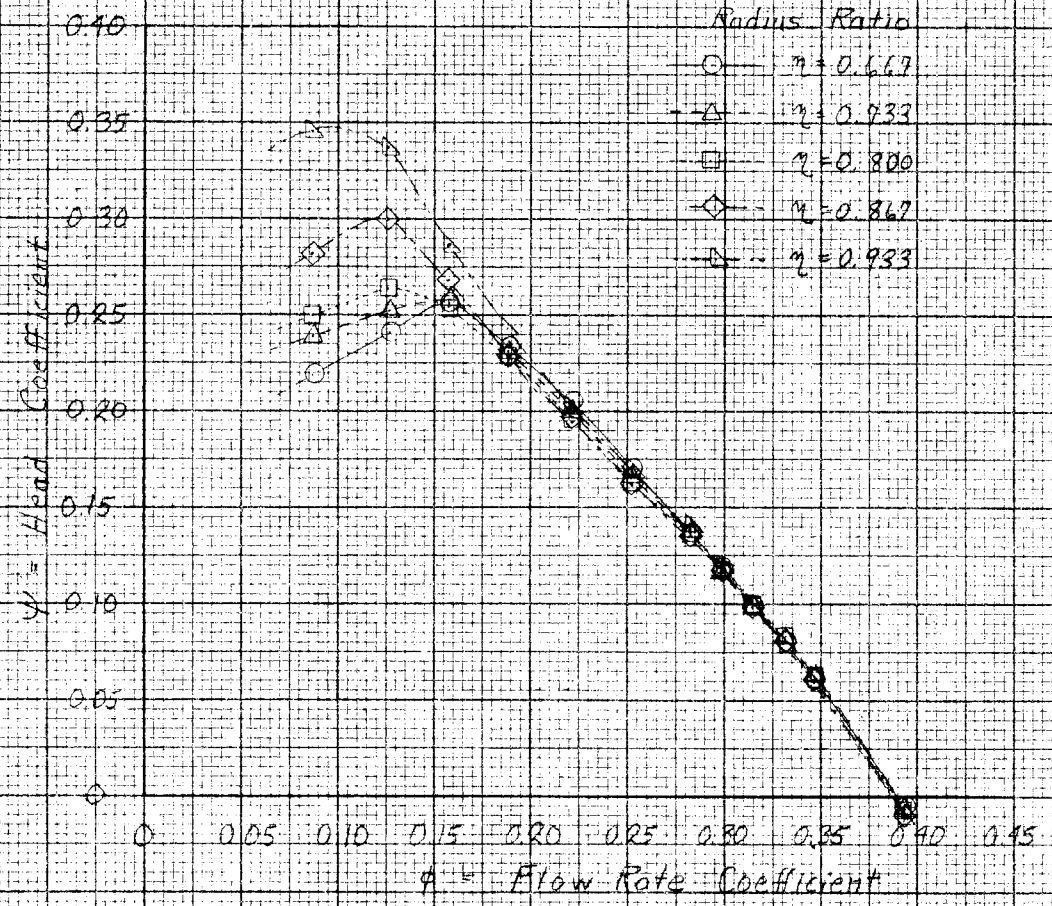

Figure 9 - Developed head coefficient measured at five radial positions.

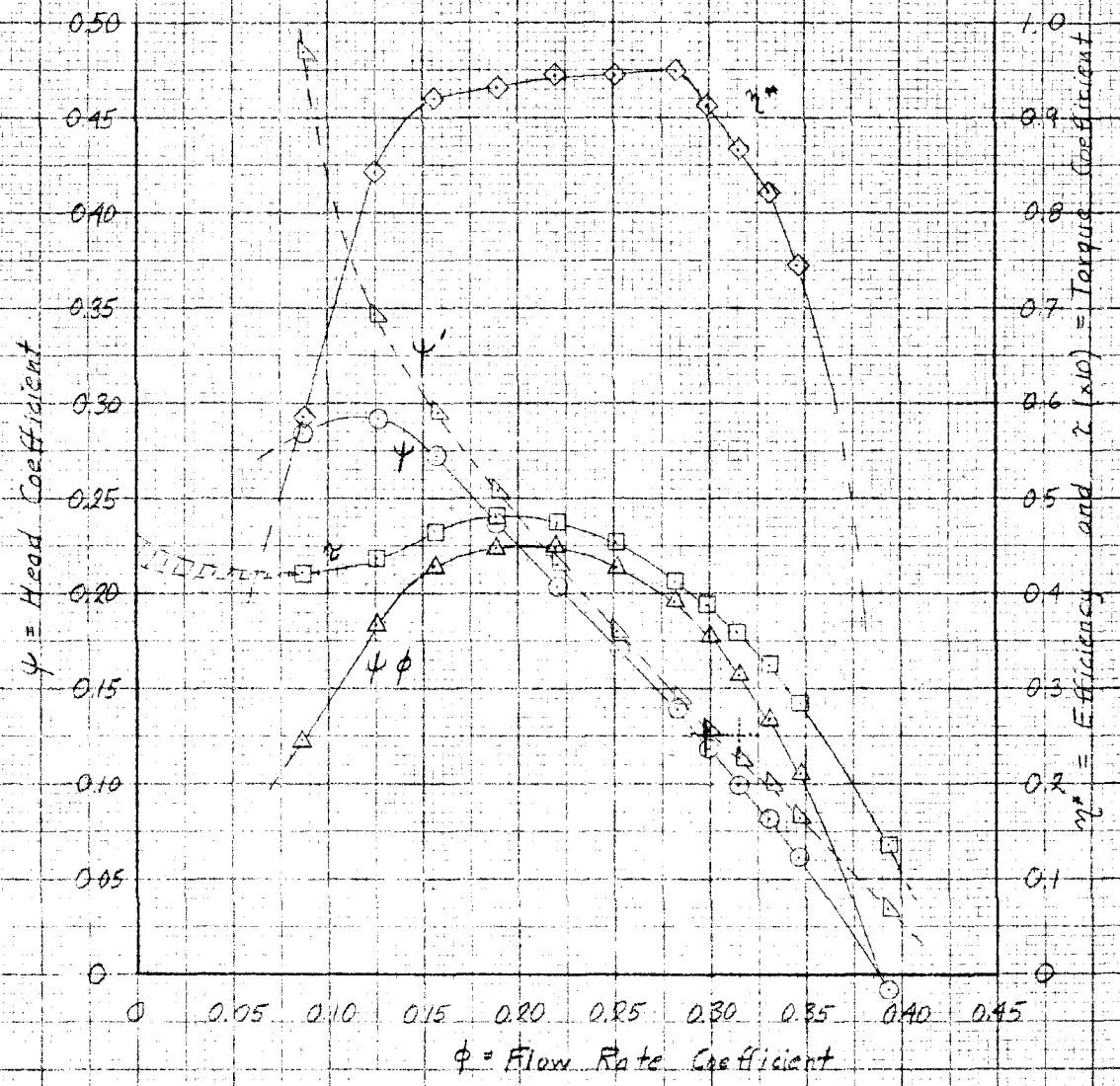

Figure 10 - Performance characteristics of the test impeller.

..... calculated design point.

—+— expected (corrected) design point.

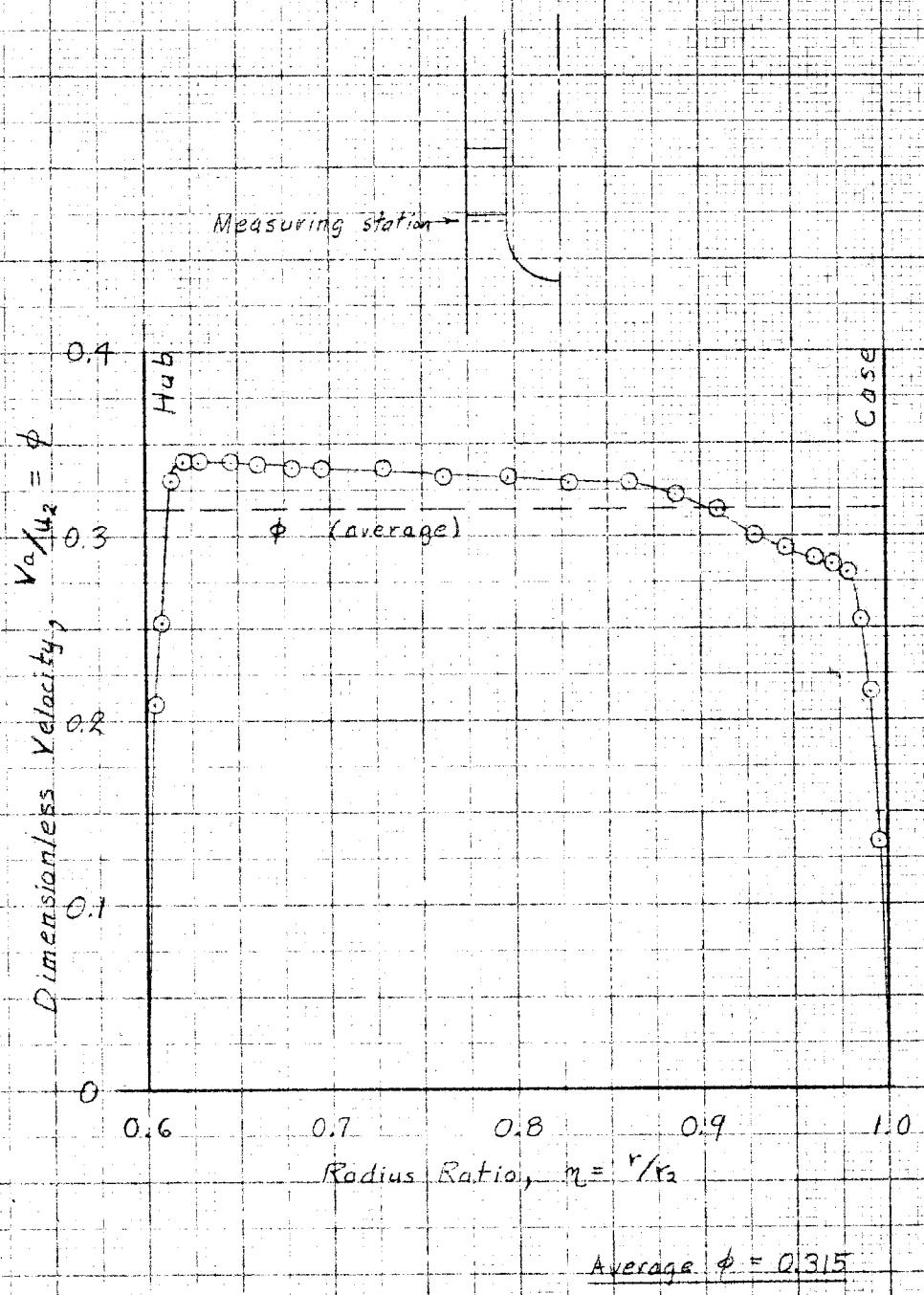

Figure 11 - Measured inlet velocity profile.

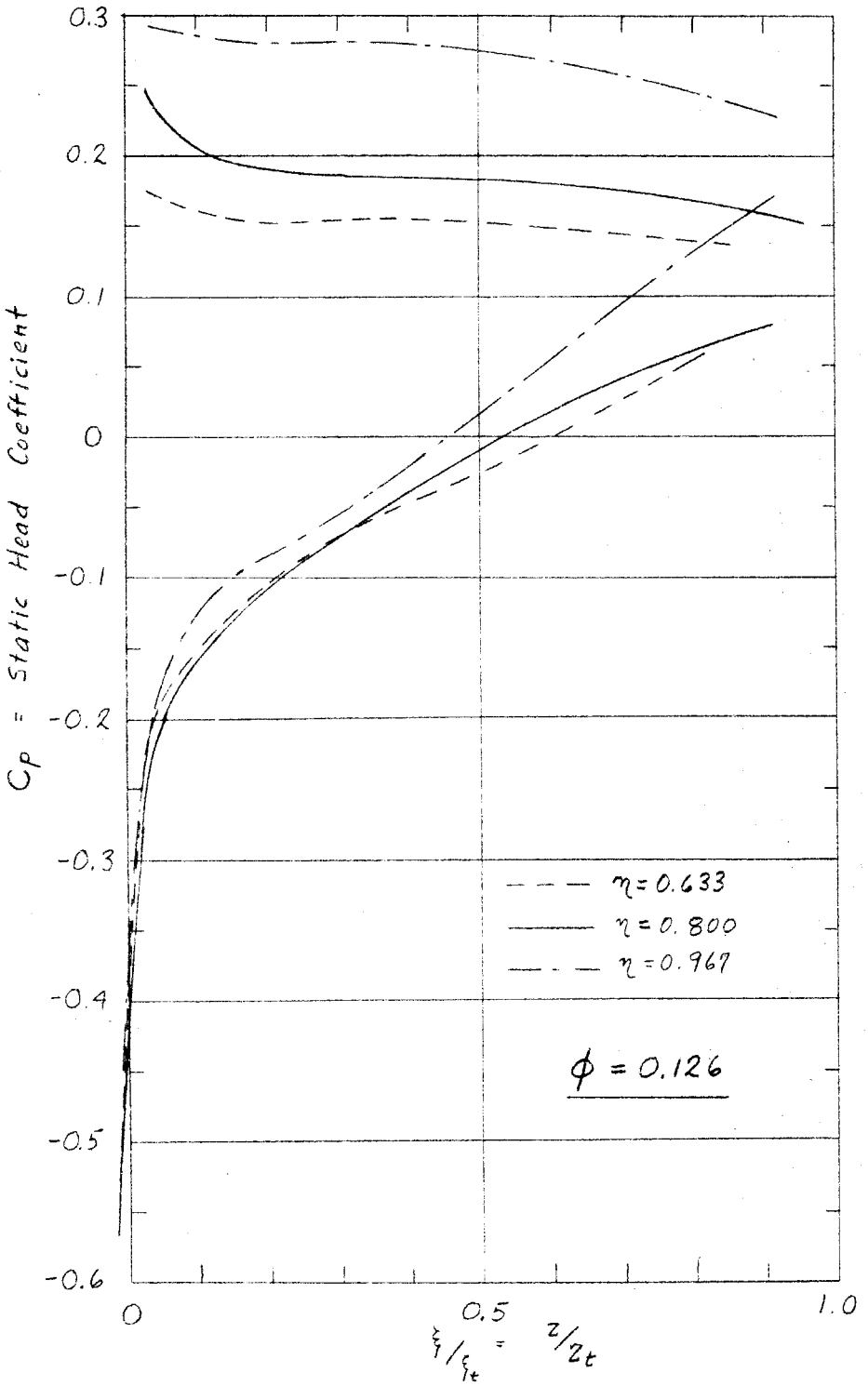

Figure 12 - Static head distributions as a function of the axial extent.

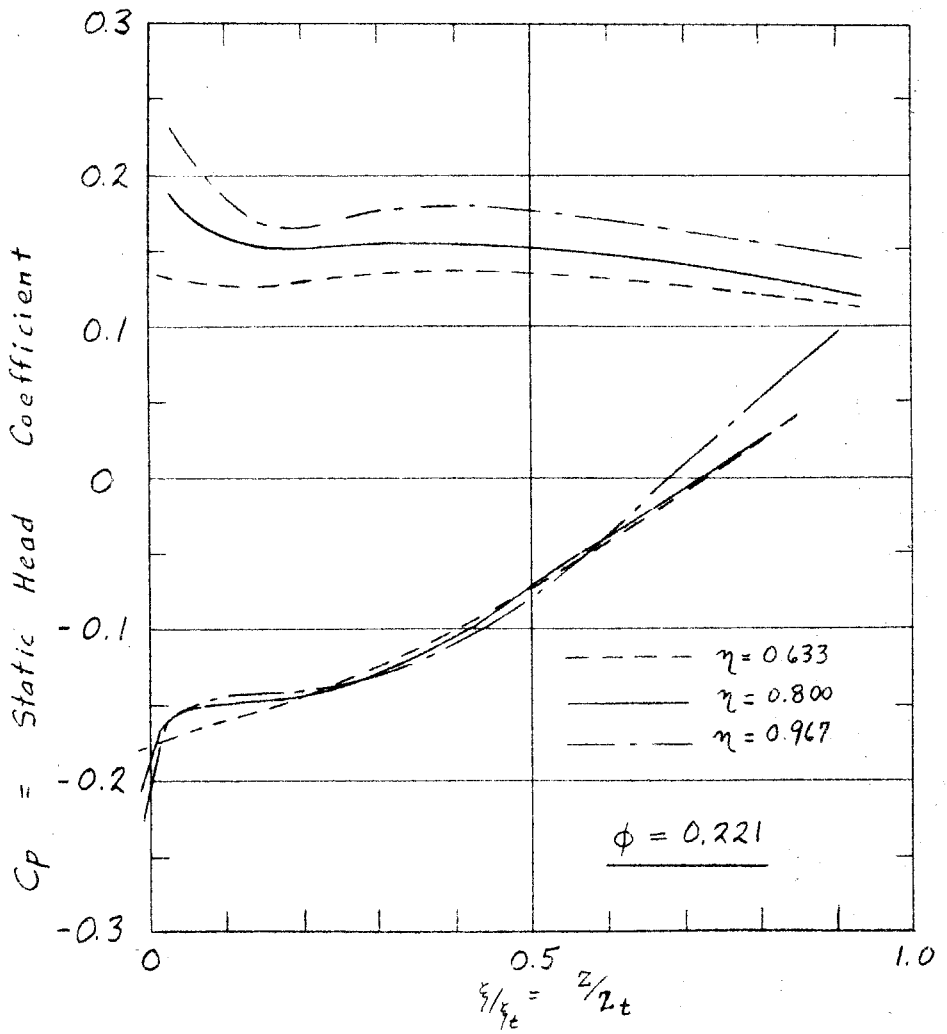

Figure 12 (continued) - Static head distributions on the blades as a function of the axial extent.

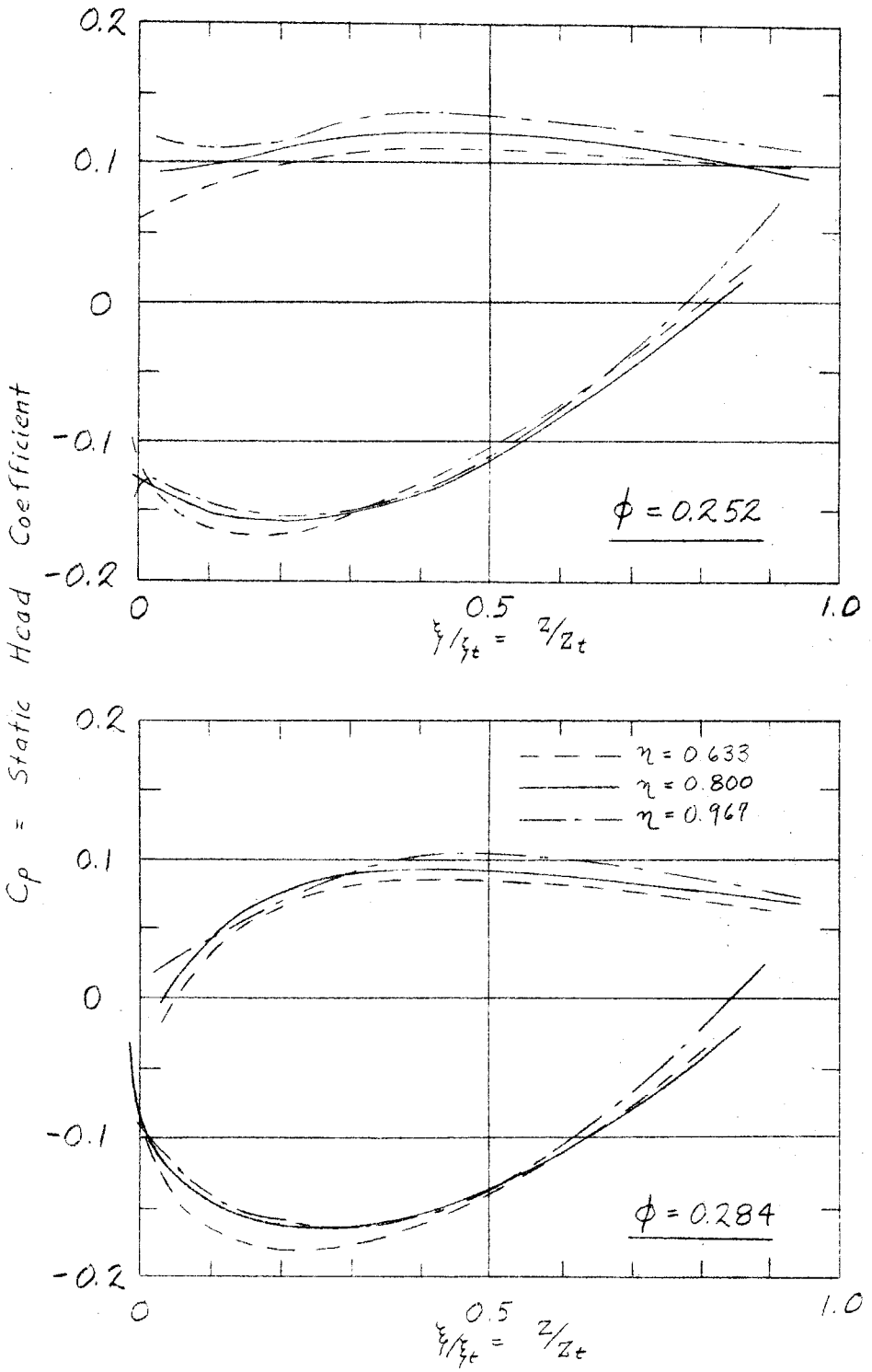

Figure 12 (continued) - Static head distributions on the blades as a function of the axial extent.

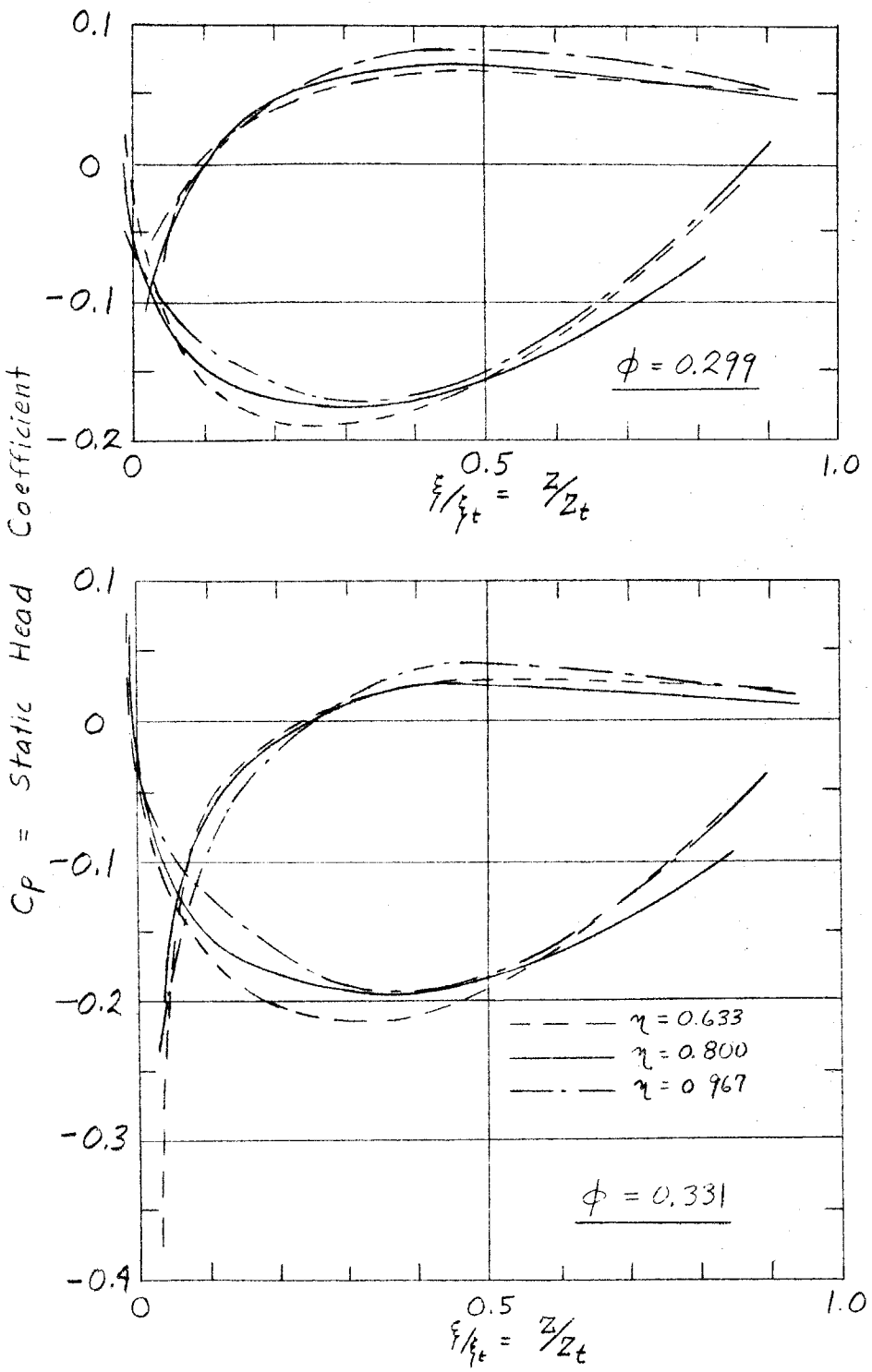

Figure 12 (concluded) - Static head distributions on the blades as a function of the axial extent.

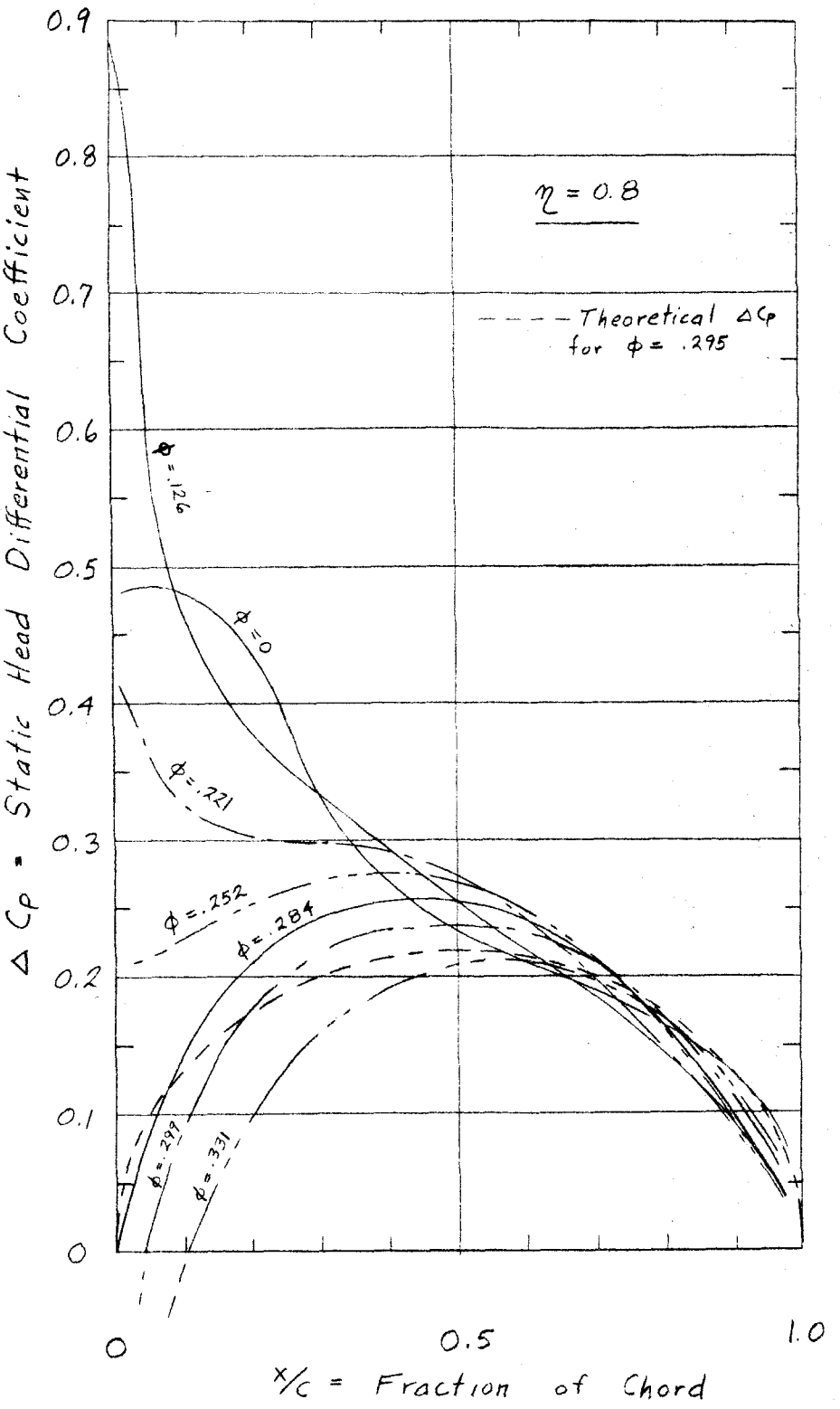

Figure 13 - Static head differentials as a function of the chord for the mid-radius position.

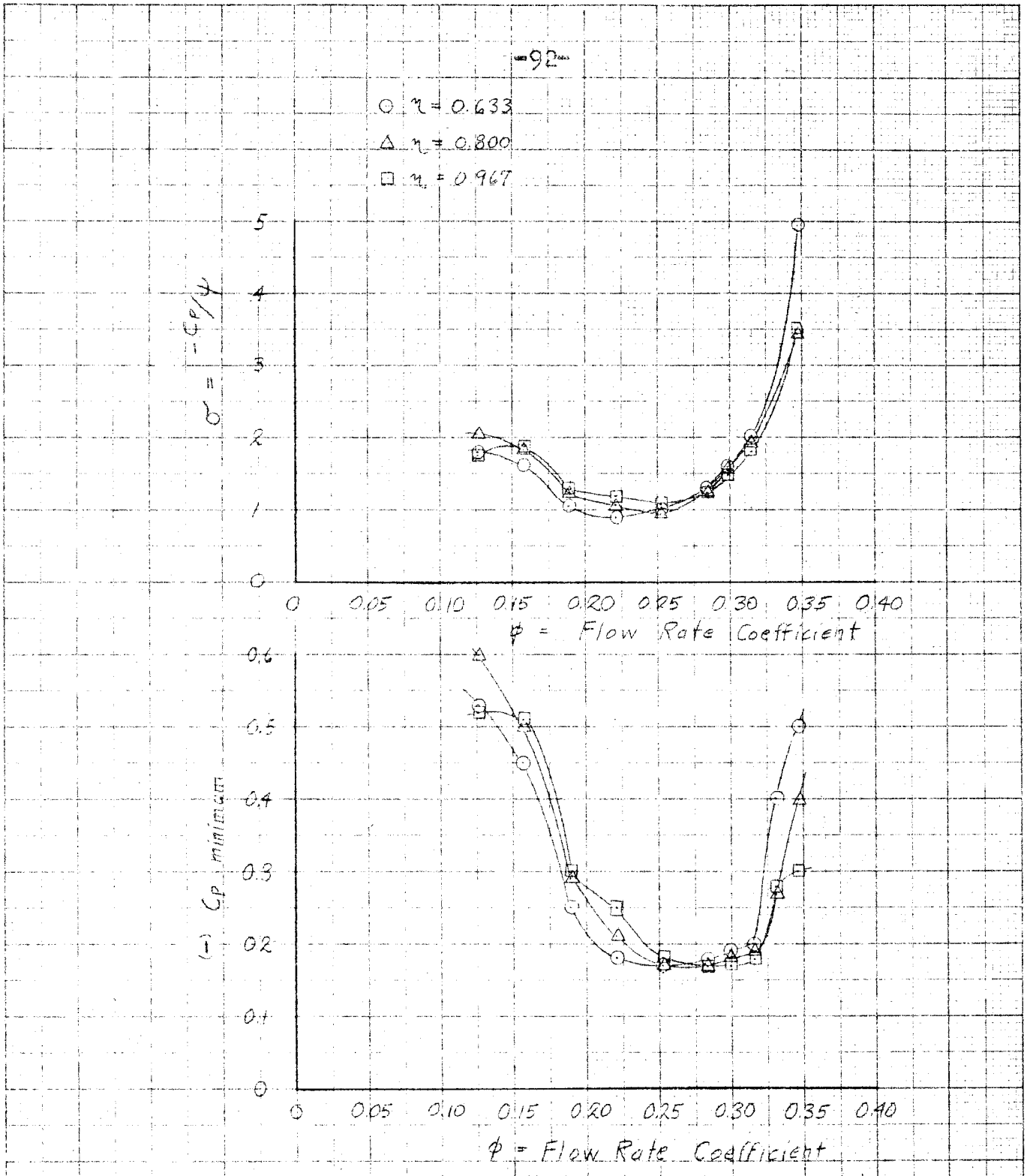

Figure 14 - Incipient cavitation coefficients determined from the static head distributions.

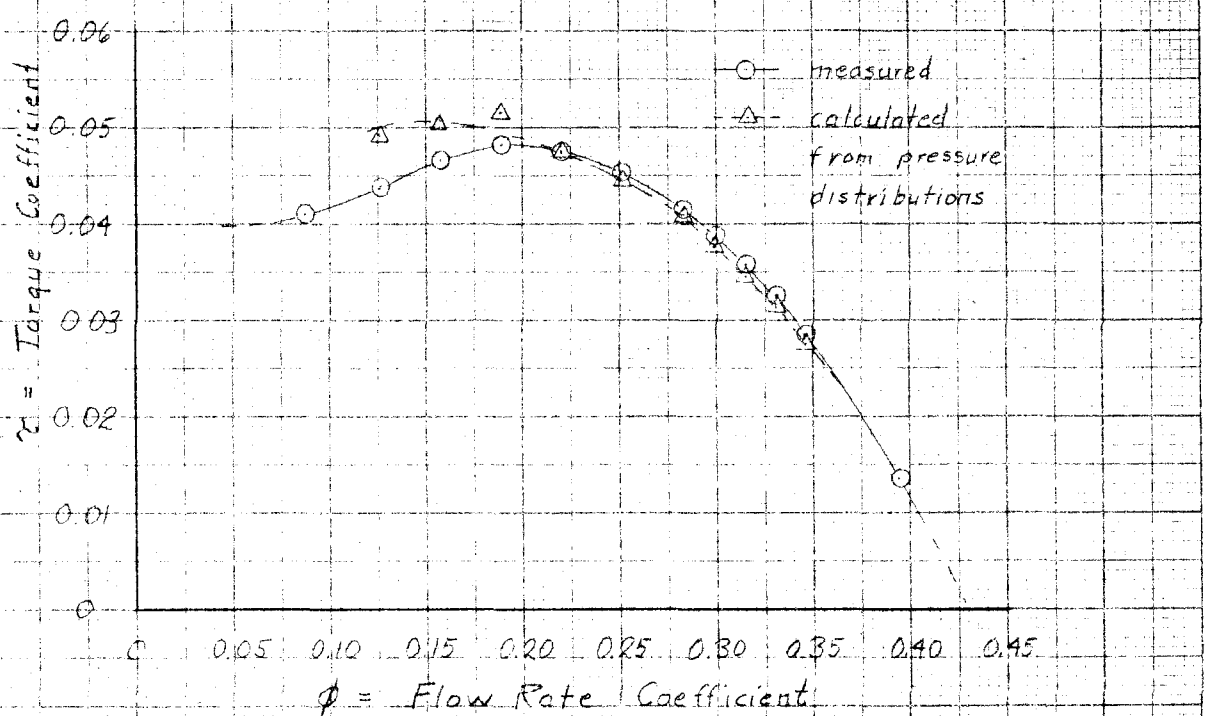

Figure 15 - Measured and calculated torque coefficients.

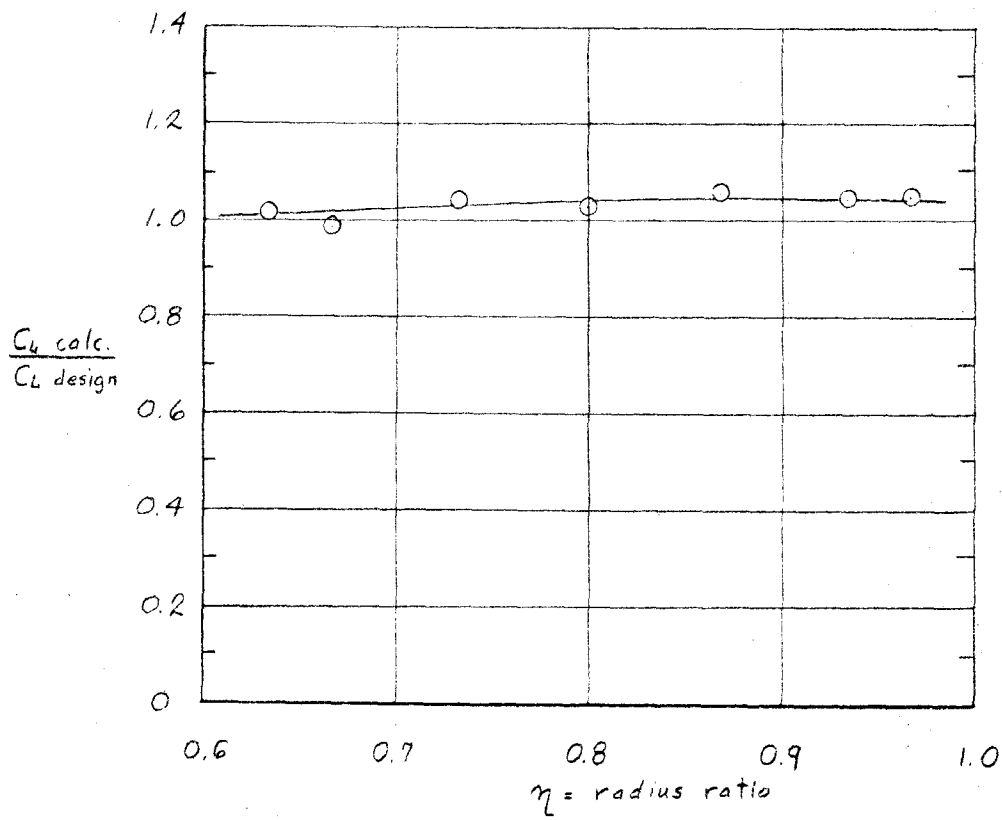

Figure 16 - Ratio of the lift coefficient calculated from the static head distributions to the design lift coefficient as a function of radius.

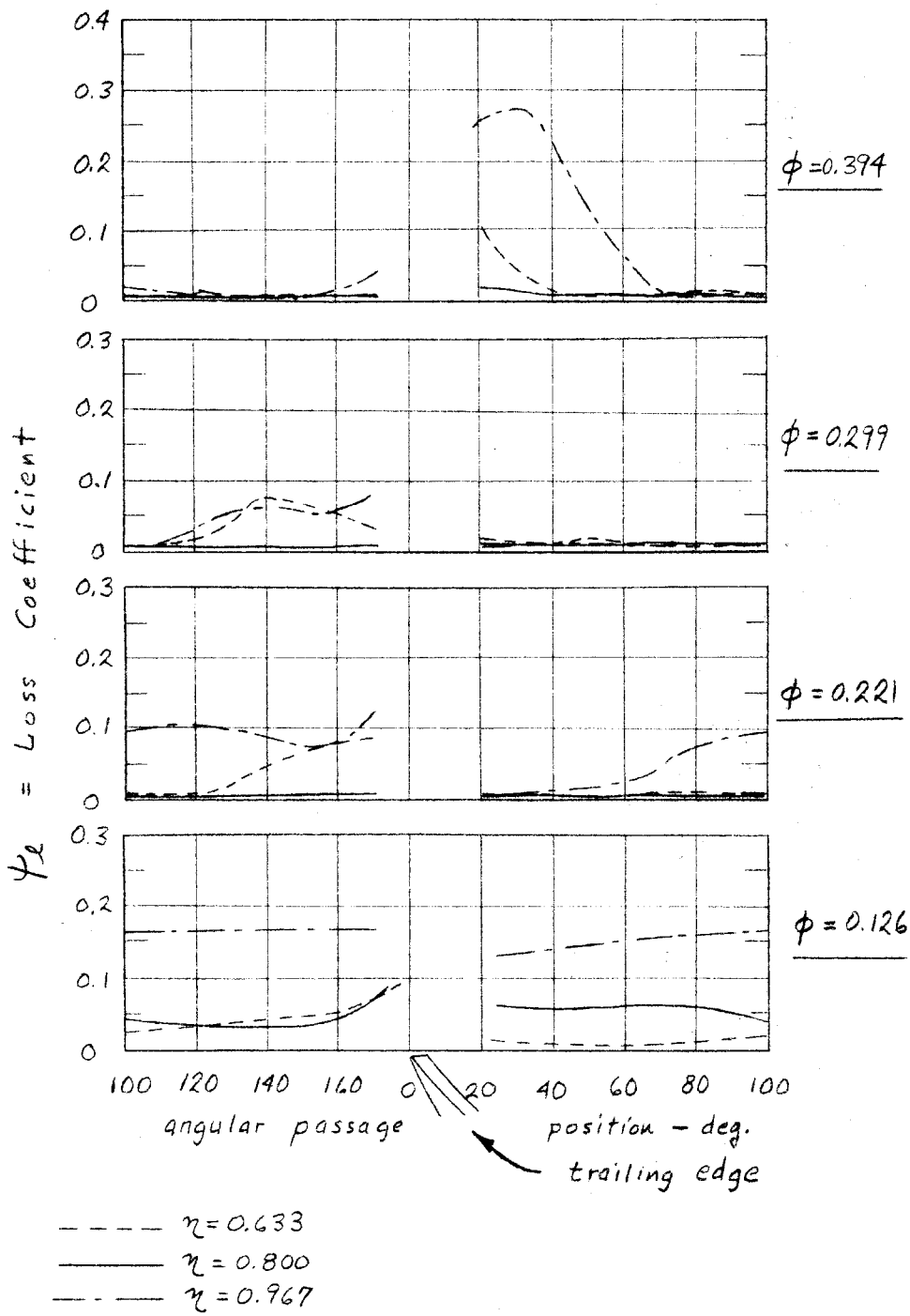

Figure 17 - Measured losses in the impeller exit area.

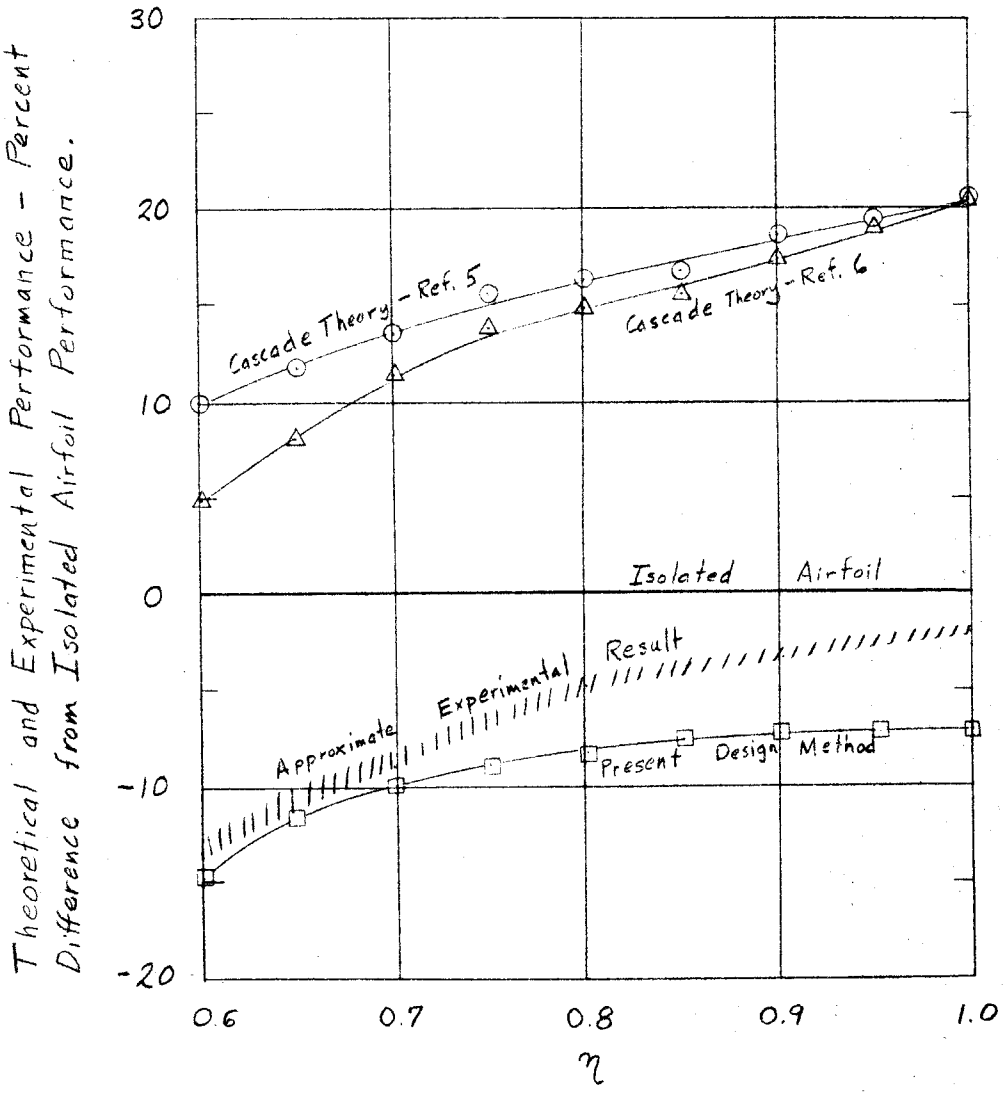

Figure 18 - Comparison of theoretical expectations and experimental result as percentages from isolated airfoil performance.